Analytical Modeling and Characterization of Electromigration Effects for Multibranch Interconnect Trees

Hai-Bao Chen, Sheldon X.-D. Tan, *Senior Member, IEEE*, Xin Huang, Taeyoung Kim, and Valeriy Sukharev

***Abstract*—Electromigration (EM) in very large scale integration (VLSI) interconnects has become one of the major reliability issues for current and future VLSI technologies. However, existing EM modeling and analysis techniques are mainly developed for a single wire. For practical VLSI chips, the elemental EM reliability unit called interconnect tree is a multibranch interconnect segment consisting of a continuously connected, highly conductive metal (Cu) lines terminated by diffusion barriers and located within the single level of metallization. The EM effects in those branches are not independent and have to be considered simultaneously. In this paper, we demonstrate, for the first time, a first principle-based analytical solution of this problem. We have derived the analytical expressions describing the hydrostatic stress evolution in several typical interconnect trees: 1) the straight-line three-terminal wires; 2) the T-shaped four-terminal wires; and 3) the cross-shaped five-terminal wires. The new approach solves the stress evolution in a multibranch tree by de-coupling the individual segments through the proper boundary conditions (BCs) accounting the interactions between different branches. By using Laplace transformation technique, analytical solutions are obtained for each type of the interconnect trees. The analytical solutions in terms of a set of auxiliary basis functions using the complementary error function agree well with the numerical analysis results. Our analysis further demonstrates that using the first two dominant basis functions can lead to 0.5% error, which is sufficient for practical EM analysis.**

***Index Terms*—Electromigration (EM), modeling and analysis, multibranch interconnect trees, stress evolution.**

Manuscript received May 17, 2015; revised July 27, 2015 and November 4, 2015; accepted November 27, 2015. Date of publication January 29, 2016; date of current version October 18, 2016. This work was supported in part by the National Science Foundation under Grant CCF-1255899, Grant CCF-1527324, and Grant CCF-1017090, in part by the Semiconductor Research Corporation under Grant 2013-TJ-2417, part by Shanghai Jiao Tong University through the 985 Research Fund, and in part by the National Natural Science Foundation of China under Grant 20873999. This paper was recommended by Associate Editor Y. Cao.

H.-B. Chen is with the Department of Micro/Nano-Electronics, Shanghai Jiao Tong University, Shanghai 200240, China (e-mail: haibaochen@sjtu.edu.cn).

S. X.-D. Tan and X. Huang are with the Department of Electrical and Computer Engineering, University of California, Riverside, CA 92521 USA (e-mail: stan@ece.ucr.edu; xhuan009@ucr.edu).

T. Kim is with the Department of Computer Science and Engineering, University of California, Riverside, CA 92521 USA (e-mail: tkim049@cs.ucr.edu).

V. Sukharev is with Mentor Graphics Corporation, Fremont, CA 94538 USA (e-mail: Valeriy_Sukharev@mentor.com).

Color versions of one or more of the figures in this paper are available online at http://ieeexplore.ieee.org.

Digital Object Identifier 10.1109/TCAD.2016.2523898

I. INTRODUCTION

ELECTROMIGRATION (EM)-INDUCED reliability becomes a major design constraint in the current and future nanometer very large scale integration (VLSI) technologies. To ensure the EM signoff, conservative design rules based on the worst cases (highest possible temperature and power consumption) and simple EM model such as Black's equation can lead to significant overdesign and 2×–3× enlarged guard bands [1]. Such conservative and overdesign rules, however, will be no longer an option in current and future technologies because 3× guard band increase will significantly increase the buffer size and many other aspects of chips, which will lead to increasing currents, and hence, the cost and power of the chips. As a result, more accurate EM modeling and analysis techniques are required to ensure sufficient accuracy without sacrificing the efficiencies.

A. *Physics-Based EM Reliability Model*

Existing EM model and analysis techniques mainly focus on the simple straight line interconnect with two-line end terminals. However, a practical integrated circuit layout often has interconnects with more complex, multibranch structures. The EM-induced stress evolutions in those branches are not independent and they have to be considered simultaneously [2], [3]. Currently, employed Blech limit [4] (for the out filtration of immortal segments) and Black's equation [5] (for calculating mean time-to-failures (MTTFs) for segments characterized by known current densities and temperatures) are subjects of the hard criticism [6], [7]. Across-die variation of residual stress makes the Blech's "critical product" to be layout-dependent variables rather than experimentally determined constants. The dependency of the Black's activation energy on the current density and temperature makes rather controversial the widely accepted methodology of calculating the MTTF at use condition. It is so because conventionally, the use activation energy and current density exponent are assumed to be the same as those determined at the stressed (accelerated) condition, characterized by high current densities and elevated temperatures.

Recently, some physics-based EM analysis methods for the through-silicon via (TSV) and power grid networks have been proposed based on solving the basic mass balance equations [8]. Since these proposed methods solve the basic mass balance equations using the finite element method, they can only solve very small structures such as one TSV. Complicated look-up table or models have to be built for different TSVs and wire segments for full-chip power grid analysis at reduced accuracy. To mitigate this problem, a novel compact physics-based EM model was proposed recently in [9] and [10]. It is based on the solution of the diffusion-like continuity equation

0278-0070 © 2016 IEEE. Personal use is permitted, but republication/redistribution requires IEEE permission.
See http://www.ieee.org/publications_standards/publications/rights/index.html for more information.

Authorized licensed use limited to: Univ of Calif Riverside. Downloaded on June 24,2026 at 15:12:23 UTC from IEEE Xplore. Restrictions apply.

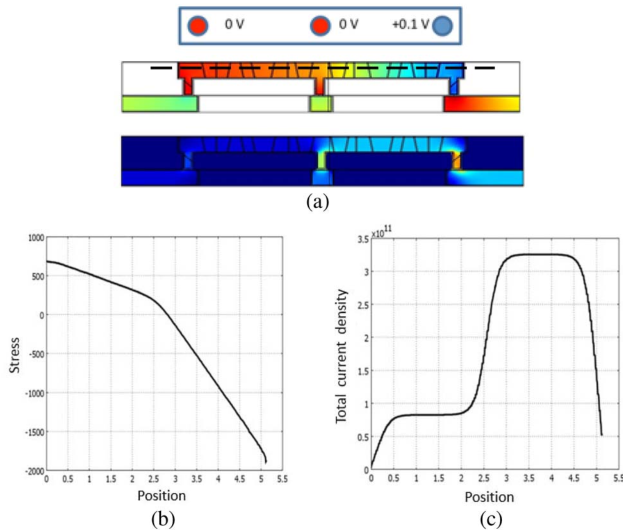

Fig. 1. (a) Color map of hydrostatic stress and current density. (b) Hydrostatic stress along the top metal line. (c) Current density distributions.

describing the kinetics of hydrostatic stress evolution [11]. Although the new EM model has been extended to deal with a multiple branch tree based on the projected steady-state stress, it still cannot provide the evolution of the hydrostatic stress, which ultimately determines the failures for multibranch interconnect wires.

To further illustrate this, Fig. 1 shows distributions of the current density and hydrostatic stress evolved in the three terminals interconnect tree loaded with DC currents. Electrons inflow the upper-level metal line through the most left and middle upstream vias and outflow to the lower-level metal line through the right downstream via. The steady state hydrostatic stress distribution, which was obtained from the solution of the linked partial differential equations (PDEs) describing the major physics of the EM phenomenon [12] with the finite element analysis tool COMSOL [13], demonstrates the two-slope stress distribution resulted by the intrabranch atom diffusion. It is clear that this stress distribution can be explained by redistribution of the atoms among both the branches of the tree. Tree decomposition on two independent segments will never explain this type of stress distribution [14]. Closed-form analytical description of the distribution of hydrostatic stress caused by EM-induced redistribution of atoms inside an interconnect tree, which is needed for determination of the potential locations for void nucleation, was the major motivation for the reported work.

B. Related Works

Many, mostly experimental studies of the EM-induced degradation of the multibranch interconnects were reported in the literature. Vairagar *et al.* [15] studied the dependence of EM-induced failure in a three-terminal Cu wire on the electric current configuration in adjoining interconnect segments and provided direct evidence of the peculiar EM behavior. Experimental characterization of the reliability of dual-damascene Cu interconnect tree structures consisting of straight contact-to-contact lines has been analyzed in [16]–[18]. However, it did not give a unified analytic form to model the three-terminal interconnect trees which strongly depend on the correlated stress evolution in neighboring segments. In [19], the effects of EM in a three-terminal L-shaped interconnect tree were studied by using a numerical simulation technique based on solution of the 1-D Korhonen's equation [11]. An analytic model for the stress evolution in the star-like tree represented by semi-infinite segments with known current densities connected at the central node has been developed in [20]. In order to implement critical threshold design rules of EM reliability, a nodal analysis technique for computing the steady-state EM-induced stress was proposed in [21]. The nodal analysis technique is an approximate method for calculating the node voltages at the ends of the interconnect segments extracted from the larger interconnect network. In [22], a systematic study of Blech effect-based model for EM in complex structures including the effect of adjacent segments has been made, but transient analysis has not been performed on this model.

In this paper, we propose, for the first time, an accurate and first principle-based analytic model for calculating the hydrostatic stress evolution in the finite multibranch interconnect trees during the void nucleation phase. An ultimate goal is a capability to predict all suspicious locations inside interconnect where void can be nucleated. A well-known steady state analysis of the hydrostatic stresses distribution across the tree can provide just potential locations for void nucleation, where these stresses exceed the critical one. In reality, when the stress evolution kinetics is considered, these void nucleation site locations could be quite different. We have derived the analytical expressions describing the hydrostatic stress evolution in several typical interconnect trees: 1) the straight-line three-terminal wires; 2) the T-shaped four-terminal wires; and 3) the cross-shaped five-terminal wires. This new approach solves the stress evolution in a multibranch tree by de-coupling the individual segments through the proper boundary condition (BC) accounting the interactions between different branches. By using Laplace transformation technique, analytical solutions are obtained for each tree. The analytical solutions then are obtained in terms of set of auxiliary basis functions using the complementary error function. The employed transient analysis is a part of the dynamical analysis of the EM-induced IR-drop degradation. Those analytical EM models agree well with COMSOL simulation results. Furthermore, we demonstrate that employing just the first dominant basis function can lead to less than 4% error and by using the first two basis functions the error does not exceed 0.5%, which is sufficient for practical EM analysis.

The rest of this paper is organized as follows. Section II describes the existing analytical expression for the stress evolution in the single confined metal line with the blocking BC. In Section III, we present our analytical solutions by using the Laplace transformation technique for the straight-line three-terminal wire, the T-shaped four-terminal wire, and the cross-shaped five-terminal wire. In Section IV, we show the segment length effect in EM-induced stress evolution by using the proposed analytical method. Experimental results for a number of benchmark examples are provided in Section V. Concluding remarks are drawn in Section VI. The details of the mathematical derivation of the analytical EM analysis for the T-shaped four-terminal interconnect tree and the cross-shaped five-terminal interconnect tree are presented in the Appendix.

II. Dynamic Stress Evaluation for Single Segment Wire

Before we present our analytical solutions to the PDE describing the stress evolution in multibranch interconnect trees, let us review the basic hydrostatic stress evolution taking place in a single segment wire loaded with the constant electric current.

Authorized licensed use limited to: Univ of Calif Riverside. Downloaded on June 24,2026 at 15:12:23 UTC from IEEE Xplore. Restrictions apply.

TABLE I
NOTATIONS AND TYPICAL VALUE IN OUR TRANSIENT SIMULATION

Term	Typical value	Description
ρ	3e-8Ω· m	Electrical resistivity
e	1.60e-19C	Electric charge
Z^*	10	Effective valence charge
Ω	8.78e-30 m^3	Atomic volume
k	1.38e-23J/K	Boltzmann constant
B	1e11Pa	Back flow stress modular
D_0	5.2e-5m^2/ s	Self-diffusion coefficient
E_a	1.1eV	Activation energy
σ_T	400MPa	Thermal stress
j	From simulation	Current density
T	From simulation	Absolute temperature
σ	From simulation	Electromigration stress

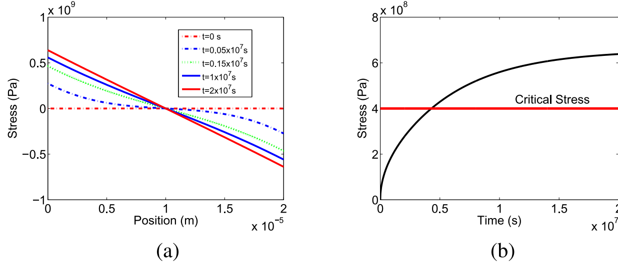

Fig. 2. (a) EM-induced stress development and distribution along a single metal wire. (b) Stress development at the cathode node.

For a 1-D metal wire, the stress evolution $\sigma(t)$ caused by EM effects is well described by the following diffusion-like equation [11]:

$$\frac{\partial \sigma(x,t)}{\partial t} = \frac{\partial}{\partial x}\left[\kappa\left(\frac{\partial \sigma(x,t)}{\partial x} + G\right)\right] \tag{1}$$

where $\kappa = (D_a B\Omega/kT)$ is the "stress" diffusivity and $G = (Eq^*/\Omega)$ is the EM driving force, D_a is the effective atomic diffusion coefficient

$$D_a = D_0 \exp\left(-\frac{E_a}{kT}\right). \tag{2}$$

Here, D_0 is the pre-exponential factor, E_a is the activation energy, B is the effective bulk modulus, Ω is the atomic volume, k is Boltzmann's constant, T is the absolute temperature, E is the electric field, and q^* is the effective charge. The electric field E can be replaced by the product of the resistivity ρ times the current density j, i.e., $E = \rho j$. The effective charge $q^* = |Z^*|e$ is a known quantity, where e is the elementary charge and Z^* is the effective charge number. As a result, driving force G can be rewritten as $G = (\rho j|Z^*|e/\Omega)$. To facilitate the comprehension of this paper, we summarize the major notations in Table I.

Fig. 2 shows the stress development over time in a metal line computed by COMSOL. Fig. 2(a) shows that tensile (the positive) stress will be developed over time at the cathode node (left node) and compressive (the negative) stress will be developed at the anode node (right node). The stress changes sign in the middle of the wire. The built-up stress (its gradient) will serve as the counter-force for atomic flux. It was agreed that development of the so-called critical stress σ_{crit} should be used as a condition for a void nucleation. Indeed, due to a huge activation energy a void cannot be nucleated by, for example, vacancy agglomeration even when the stress is big. At the same time different natural flaws such as micro cracks, small process induced cavities (pores), dislocation gladding induced steps, etc., usually pre-exist in metal. The classical model of the homogeneous nucleation [23] says that a cavity located in the metal, loaded with the hydrostatic tensile stress σ, can either shrink or enlarge depending on the original cavity size R. In the very rough approximation, which we use for illustrative purposes, if $R < R_c = 2\gamma/\sigma$, where γ is the cavity surface energy per unit area, the cavity will shrink to reduce the free energy of the system represented by the metal with cavity; if $R > R_c$, the cavity will enlarge to reduce this energy. Thus, assuming that the pre-existing cavities are of the 5–10 nm size, we can estimate the critical stress level of $\sigma \approx 200$–500 MPa when $\gamma = 1N/m^2$. It means, if stress exceeds the critical level then the pre-existing cavities of the corresponding sizes start to grow. Rate of this growth is determined by the atomic diffusion, i.e., is pretty slow. We can see from Fig. 2(b) that if the largest stress at the cathode node exceeds the critical stress, then the growing voids will be generated. If the stress development enters a steady state (atomic diffusion stops) before it reaches the critical stress, the wire will become immortal.

Equation (1) can have different closed-form solutions with different BC. Following [11], we assume throughout the rest of this paper that the diffusivity-like parameter κ does not depend on stress, and hence, on time. For the blocking BC, the atomic flux is blocked at both line ends $x = 0$ and $x = L$, i.e., $J(0,t) = J(L,t) = 0$, where $J(x,t) = (D_a/\Omega kT)((\partial\sigma(x,t)/\partial x) + G)$. Following [11], the stress evolution in the line can be described as

$$\sigma(x,t,\kappa,G) = \sigma_T + GL\left\{\frac{1}{2} - \frac{x}{L} - 4\sum_{n=0}^{\infty}\frac{\cos\left((2n+1)\pi\frac{x}{L}\right)}{(2n+1)^2\pi^2\exp\left((2n+1)^2\pi^2\frac{\kappa t}{L^2}\right)}\right\} \tag{3}$$

where σ_T is the pre-existing residual stress due to a thermal process. An ultimate target of the existing EM modeling approaches is prediction of the void nucleation time, i.e., the instance in time when the stress developed in the line has reached the critical stress [24]. To derive the closed-form expression, one can keep the slowest decaying term of the infinite series in (3) to obtain the approximate estimation for stress at the line cathode end ($x = 0$) as

$$\sigma(t,T,j) \approx \sigma_T + GL\left(\frac{1}{2} - \frac{1}{2\exp\left\{\frac{D_a B\Omega t}{L^2 kT}\right\}}\right). \tag{4}$$

As a result, when $\sigma(t,T,j) \geq \sigma_{\text{crit}}$, the nucleation time t_{nuc} can be computed in an analytical form as

$$t_{\text{nuc}} = \frac{L^2 kT}{D_a B\Omega}\ln\left\{\frac{\frac{\rho j|Z^*|eL}{2\Omega}}{\sigma_T + \frac{\rho j|Z^*|eL}{2\Omega} - \sigma_{\text{crit}}}\right\}. \tag{5}$$

III. NEW ANALYTICAL MODELS FOR MULTIBRANCH INTERCONNECT TREE

In this section, we present our analytical solution to the multibranch interconnect trees. We discuss three cases: 1) the

Authorized licensed use limited to: Univ of Calif Riverside. Downloaded on June 24,2026 at 15:12:23 UTC from IEEE Xplore. Restrictions apply.

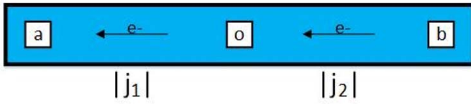

Fig. 3. Straight-line three-terminal interconnect tree.

straight-line three-terminal interconnect tree; 2) the T-shaped four-terminal interconnect tree; and 3) the cross-shaped five-terminal interconnect tree as they are commonly seen in many practical VLSI wirings for a single metal layer. In this paper, the tree is defined as an elemental EM reliability unit consisting of continuously connected highly conductive metal segments lying within one layer of metallization and surrounded by the diffusion barriers [Ta/TaN liners and Si(C)N dielectric barrier]. In the general case the tree has more than one termination branch. In this section, we focus on the three cases, corresponding to different types of trees, regarding the derivation of exact analytical solutions and approximate expressions for the hydrostatic stress evaluation in the EM void nucleation phase.

A. Straight-Line Three-Terminal Interconnect Tree

For multibranch interconnect tree, EM-induced stress evolution in nucleation and growth phases is still governed by the Korhonen's equation [11]. But it is a difficult task to solve simultaneously the Korhonen's equation for all the branches. One viable approach is to break the multibranch interconnect tree into a number of simple single-segment wires in a way that we can apply the Korhonen's equation for each segment. At the joints of two connected wire segments, the stress value must be continuous as well as the atomic flux. It should be noted that the last condition is valid in the case of equal segment widths, which is analyzed below. Also, note that the current densities at the boundaries may not be continuous, but must meet the Kirchhoff's circuit law.

We first analyze the three-terminal interconnect tree with two segments with the current flow directions as shown in Fig. 3. The current densities in the two segments may not be the same, which will be determined by the rest of the circuit. For the two segments, we have the following two diffusion equations based on the Korhonen model [11]:

$$\begin{aligned}\frac{\partial\sigma_1(x,t)}{\partial t} &= \frac{\partial}{\partial x}\left[\kappa_1\left(\frac{\partial\sigma_1(x,t)}{\partial x}+G_1\right)\right],\\ &\qquad \texttt{in } -L<x<0,\ t>0\\ \frac{\partial\sigma_2(x,t)}{\partial t} &= \frac{\partial}{\partial x}\left[\kappa_2\left(\frac{\partial\sigma_2(x,t)}{\partial x}+G_2\right)\right],\\ &\qquad \texttt{in } 0<x<L,\ t>0.\end{aligned}\tag{6}$$

For the void nucleation phase, the hydrostatic stresses in the two segments will interplay with each other, which is reflected in the BC

$$\begin{aligned}&\kappa_1\left(\frac{\partial\sigma_1(x,t)}{\partial x}+G_1\right)=0,\ \texttt{at } x=-L,\ t>0\\ &\sigma_1(x,t)=\sigma_2(x,t),\ \texttt{at } x=0,\ t>0\\ &\kappa_1\left(\frac{\partial\sigma_1(x,t)}{\partial x}+G_1\right)=\kappa_2\left(\frac{\partial\sigma_2(x,t)}{\partial x}+G_2\right),\\ &\qquad \texttt{at } x=0,\ t>0\\ &\kappa_2\left(\frac{\partial\sigma_2(x,t)}{\partial x}+G_2\right)=0,\ \texttt{at } x=L,\ t>0.\end{aligned}\tag{7}$$

The second equation in (7) means that stresses at the boundary need to be continuous. The third one indicates that the atom flux is also continuous at the boundary. The ICs of the equations are as follows:

$$\begin{aligned}&\sigma_1(x,t)=0,\ \texttt{for } t=0, \texttt{in } -L<x<0\\ &\sigma_2(x,t)=0,\ \texttt{for } t=0, \texttt{in } 0<x<L\end{aligned}\tag{8}$$

which basically says that there is no stress anywhere in the whole tree at $t=0$. With the given boundary and initial conditions (ICs), it turns out that we can use the Laplace transform technique to obtain the exact analytical solution for the stresses in these two segments, which are expressed as infinite series of some basis functions.

Starting with the function $\sigma(x,t)$ of time and space coordinates, the Laplace transform of $\sigma(x,t)$ can be defined as $\hat{\sigma}(x,s) = \int_0^{+\infty} e^{-st}\sigma(x,t)dt$. This new function has several important properties which will turn out to be convenient for purposes of solving the diffusion equations (6) with the BC (7) and the IC (8). The Laplace transform technique has been used to calculate the hydrostatic stress evolution at the intersection of a semi-infinite interconnect [18], [20]. However, they did not give an exact closed-form expression of the stress evolution of this type of interconnect if each segment has finite length. Using this Laplace transform for (6) with the IC (8), we get the ordinary differential equations

$$\begin{aligned}\frac{d^2\hat{\sigma}_1(x,s)}{dx^2} &= \frac{s}{\kappa_1}\hat{\sigma}_1(x,s),\ -L<x<0\\ \frac{d^2\hat{\sigma}_2(x,s)}{dx^2} &= \frac{s}{\kappa_2}\hat{\sigma}_2(x,s),\ 0<x<L.\end{aligned}\tag{9}$$

Solution of these equations provides

$$\begin{aligned}\hat{\sigma}_1(x,s) &= A_{1,I}e^{\sqrt{\frac{s}{\kappa_1}}x}+B_{1,I}e^{-\sqrt{\frac{s}{\kappa_1}}x}\\ \hat{\sigma}_2(x,s) &= A_{2,I}e^{\sqrt{\frac{s}{\kappa_2}}x}+B_{2,I}e^{-\sqrt{\frac{s}{\kappa_2}}x}.\end{aligned}\tag{10}$$

We will need to calculate the undetermined coefficients $A_{1,I}$, $A_{2,I}$, $B_{1,I}$, and $B_{2,I}$ so that the corresponding solutions satisfy the BC (7). Using the Laplace transform again, we get

$$\begin{aligned}&\frac{d\hat{\sigma}_1(x,s)}{dx}+\frac{G_1}{s}=0,\ \texttt{at } x=-L\\ &\sigma_1(x,s)=\sigma_2(x,s),\ \texttt{at } x=0\\ &\kappa_1\left(\frac{d\hat{\sigma}_1(x,s)}{dx}+\frac{G_1}{s}\right)=\kappa_2\left(\frac{d\hat{\sigma}_2(x,s)}{dx}+\frac{G_2}{s}\right),\ \texttt{at } x=0\\ &\frac{d\hat{\sigma}_2(x,s)}{dx}+\frac{G_2}{s}=0,\ \texttt{at } x=L.\end{aligned}\tag{11}$$

Substituting the expressions $\hat{\sigma}_1(x,s)$ and $\hat{\sigma}_2(x,s)$ from (10) into (11), we obtain

$$\begin{bmatrix}\frac{a_1}{d_1} & -a_1d_1 & 0 & 0\\ 0 & 0 & a_2d_2 & -\frac{a_2}{d_2}\\ \kappa_1a_1 & -\kappa_1a_1 & -\kappa_2a_2 & \kappa_2a_2\\ 1 & 1 & -1 & -1\end{bmatrix}\begin{bmatrix}A_{1,I}\\ B_{1,I}\\ A_{2,I}\\ B_{2,I}\end{bmatrix}=\begin{bmatrix}-c_1\\ -c_2\\ f_{21}\\ 0\end{bmatrix}\tag{12}$$

where $a_i=\sqrt{(s/\kappa_i)}$, $b_i=a_iL$, $c_i=(G_i/s)$, $d_i=e^{b_i}(i=1,2)$, and $f_{21}=\kappa_2c_2-\kappa_1c_1$.

Solution of the linear system (12) yields these coefficients. For the sake of simplicity we assume that each branch in

Authorized licensed use limited to: Univ of Calif Riverside. Downloaded on June 24,2026 at 15:12:23 UTC from IEEE Xplore. Restrictions apply.

the three-terminal interconnect tree has the same diffusivity, i.e., $\kappa_1 = \kappa_2 = \kappa$. In order to ensure that this assumption is met, the temperature for each branch should be kept the same due to the fact that the diffusion coefficient in metal (Cu) lines depends on the temperature. With this assumption, we can conclude that $a_1 = a_2 = a$, $b_1 = b_2 = b$, and $d_1 = d_2 = d$. Thus, solving the linear system (12) yields

$$\begin{aligned}
A_{1,I} &= \frac{2c_1 d^{-3} - (c_1 - c_2)d^{-2} - 2c_2 d^{-1} - (c_1 - c_2)}{2a(1 - d^{-4})} \\
B_{1,I} &= \frac{-(c_1 - c_2)d^{-4} - 2c_2 d^{-3} - (c_1 - c_2)d^{-2} + 2c_1 d^{-1}}{2a(1 - d^{-4})} \\
A_{2,I} &= \frac{-(c_1 - c_2)d^{-4} + 2c_1 d^{-3} - (c_1 - c_2)d^{-2} - 2c_2 d^{-1}}{2a(1 - d^{-4})} \\
B_{2,I} &= \frac{-2c_2 d^{-3} - (c_1 - c_2)d^{-2} + 2c_1 d^{-1} - (c_1 - c_2)}{2a(1 - d^{-4})}.
\end{aligned} \tag{13}$$

In order to derive the analytical solutions $\sigma_1(x,t)$ and $\sigma_2(x,t)$ from (10) and (13) by using the inverse Laplace transform technique, we need to introduce the following functions:

$$\begin{aligned}
&\xi_1(x,n) = (3+4n)L - x, \;\; \xi_2(x,n) = (2+4n)L - x \\
&\xi_3(x,n) = (1+4n)L - x, \;\; \xi_4(x,n) = 4nL - x \\
&\xi_5(x,n) = (4+4n)L + x, \;\; \xi_6(x,n) = (3+4n)L + x \\
&\xi_7(x,n) = (2+4n)L + x, \;\; \xi_8(x,n) = (1+4n)L + x \\
&\eta_1(x,n) = (4+4n)L - x, \;\; \eta_2(x,n) = (3+4n)L - x \\
&\eta_3(x,n) = (2+4n)L - x, \;\; \eta_4(x,n) = (1+4n)L - x \\
&\eta_5(x,n) = (3+4n)L + x, \;\; \eta_6(x,n) = (2+4n)L + x \\
&\eta_7(x,n) = (1+4n)L + x, \;\; \eta_8(x,n) = 4nL + x
\end{aligned} \tag{14}$$

where n is a non-negative integer. Also we need to introduce the complementary error function which is defined as

$$\mathtt{erfc}\{x\} = \frac{2}{\sqrt{\pi}} \int_x^{+\infty} e^{-t^2} dt. \tag{15}$$

Based on the above complementary error function, we construct the following basis function:

$$g(x,t) = 2\sqrt{\frac{\kappa t}{\pi}} e^{-\frac{x^2}{4\kappa t}} - x \times \mathtt{erfc}\left\{\frac{x}{2\sqrt{\kappa t}}\right\}. \tag{16}$$

Using these functions $\xi_i(x,n)$, $\eta_i(x,n)(i = 1, 2, \ldots, 8)$ and $g(x,t)$, we can obtain the exact analytical solutions for the stress evolution in both segments

$$\begin{aligned}
\sigma_{1,I}(x,t) = &\frac{1}{2}\sum_{n=0}^{+\infty}\big\{2G_1 g(\xi_1,t) + (G_2 - G_1)g(\xi_2,t) \\
&\quad - 2G_2 g(\xi_3,t) + (G_2 - G_1)g(\xi_4,t)\big\} \\
&+ \frac{1}{2}\sum_{n=0}^{+\infty}\big\{(G_2 - G_1)g(\xi_5,t) - 2G_2 g(\xi_6,t) \\
&\quad + (G_2 - G_1)g(\xi_7,t) + 2G_1 g(\xi_8,t)\big\}
\end{aligned} \tag{17}$$

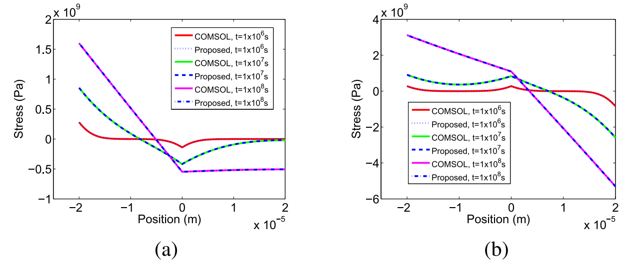

Fig. 4. EM stress development along the lines 1 and 2 in the three-terminal interconnect tree. (a) $j_1 = 2 \times 10^{10}$ A/m^2 and $j_2 = 0$ A/m^2. (b) $j_1 = 2 \times 10^{10}$ A/m^2 and $j_2 = 6 \times 10^{10}$ A/m^2.

$$\begin{aligned}
\sigma_{2,I}(x,t) = &\frac{1}{2}\sum_{n=0}^{+\infty}\big\{(G_2 - G_1)g(\eta_1,t) + 2G_1 g(\eta_2,t) \\
&\quad + (G_2 - G_1)g(\eta_3,t) - 2G_2 g(\eta_4,t)\big\} \\
&+ \frac{1}{2}\sum_{n=0}^{+\infty}\big\{-2G_2 g(\eta_5,t) + (G_2 - G_1)g(\eta_6,t) \\
&\quad + 2G_1 g(\eta_7,t) + (G_2 - G_1)g(\eta_8,t)\big\}.
\end{aligned} \tag{18}$$

As it will be shown below, if we keep the first dominant term ($n = 0$), the error is just about 4%. The approximate solutions with only one dominant term for the segments 1 and 2 are

$$\begin{aligned}
\sigma_{1,I}(x,t) \approx &\frac{1}{2}\big\{2G_1 g(\xi_1(x,0),t) + (G_2 - G_1)g(\xi_2(x,0),t) \\
&\quad - 2G_2 g(\xi_3(x,0),t) + (G_2 - G_1)g(\xi_4(x,0),t)\big\} \\
&+ \frac{1}{2}\big\{(G_2 - G_1)g(\xi_5(x,0),t) - 2G_2 g(\xi_6(x,0),t) \\
&\quad + (G_2 - G_1)g(\xi_7(x,0),t) + 2G_1 g(\xi_8(x,0),t)\big\}
\end{aligned} \tag{19}$$

$$\begin{aligned}
\sigma_{2,I}(x,t) \approx &\frac{1}{2}\big\{(G_2 - G_1)g(\eta_1(x,0),t) + 2G_1 g(\eta_2(x,0),t) \\
&\quad + (G_2 - G_1)g(\eta_3(x,0),t) - 2G_2 g(\eta_4(x,0),t)\big\} \\
&+ \frac{1}{2}\big\{-2G_2 g(\eta_5(x,0),t) + (G_2 - G_1)g(\eta_6(x,0),t) \\
&\quad + 2G_1 g(\eta_7(x,0),t) + (G_2 - G_1)g(\eta_8(x,0),t)\big\}.
\end{aligned} \tag{20}$$

Fig. 4(a) shows obtained evolution of the stress distribution along the three-terminal interconnect tree. Analytical solution obtained with the proposed method fits well to the results of the numerical simulation at every time instance. In this case, the segment 1 (left) is called reservoir as it supplies atoms to the segment 2 (right), which is called sink [21]. Typically when the current in the sink is zero or small, voids are only nucleated in the reservoir. This is clarified in Fig. 4(a), since the tensile stresses are generated in the reservoir only. But, when the sink becomes active (loaded with nonzero current), voids can be nucleated in the sink as well. In this case, the stress in some portions of the sink may exceed the critical stress that can explain the experimental observation described in [25].

Similar to the single wire case, if the critical stress σ_{crit} is known, then the void nucleation time t_{nuc} can be calculated for each segment

$$\begin{aligned}
\sigma_{1,I}(x, t_{\text{nuc},1}) &= \sigma_{\text{crit}} \\
\sigma_{2,I}(x, t_{\text{nuc},2}) &= \sigma_{\text{crit}}.
\end{aligned} \tag{21}$$

Authorized licensed use limited to: Univ of Calif Riverside. Downloaded on June 24,2026 at 15:12:23 UTC from IEEE Xplore. Restrictions apply.

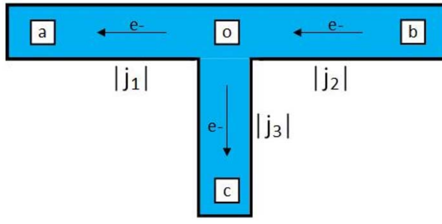

Fig. 5. T-shaped four-terminal interconnect tree.

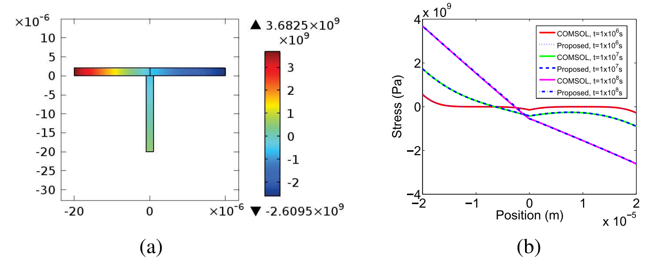

Fig. 6. (a) EM stress distribution in the T-shaped four-terminal wires at the time $t = 1 \times 10^8$ s. (b) EM stress development along the lines 1 and 2: $j_1 = 4 \times 10^{10}$ A/m^2, $j_2 = 2 \times 10^{10}$ A/m^2 and $j_3 = 1 \times 10^{10}$ A/m^2.

Since $\sigma_{1,I}(x, t_{\text{nuc},1})$ and $\sigma_{2,I}(x, t_{\text{nuc},2})$ are nonlinear functions, an iterative method can be used to find the t_{nuc}. In practical computation of the void nucleation time t_{nuc}, the complementary function can be approximated as $\texttt{erfc}\{x\} \approx (e^{-x^2}/\sqrt{\pi}x)(1 - (1/2x^2))$. Substituting this approximate form into the basis function (16), we obtain

$$g(x, t) \approx \frac{4\kappa t}{x^2}\sqrt{\frac{\kappa t}{\pi}}e^{-\frac{x^2}{4\kappa t}}. \tag{22}$$

Thus, a simplified formula for calculating the void nucleation time can be obtained from (19)–(22). Based on this simplified form, the void nucleation time can be computed by using Newton's iterative method with an initial guess which is close to the true value. Fig. 4(a) and (b) indicates that the initial estimate can be set to be about 10^7 s, which can lead to a much faster convergence.

B. T-Shaped Four-Terminal Interconnect Tree

The structure of the T-shaped four-terminal interconnect tree is shown in Fig. 5. In this case, we have three segments which connect through the middle node "o." The stress evolution equations for this interconnect tree consisting of three lines with the corresponding boundary and ICs can be solved. The dynamic stress evolution equation with BC for the T-shaped four-terminal interconnect tree can be found in the Appendix. To calculate the exact analytical solutions by using the Laplace transform technique, we need to assume that every branch in this interconnect tree has the same temperature. The details for deriving the analytical solutions has been given in the Appendix and here we only show the final results.

As it was done in the previous case of the two-terminal stress, the analytical solution is represented in terms of a set of auxiliary basis functions by using the complementary error function. Practical calculation formulas should be developed for the exact series solutions of the four-terminal interconnect tree. Below we will demonstrate that the first dominant term is a good approximate solution

$$\begin{aligned}\sigma_{1,T}(x_1, t) &\approx -\frac{1}{3}\big\{-3G_1 g(\xi_1(x_1,0),t) + (G_1 - G_2 + G_3)g(\xi_2(x_1,0),t)\\ &\quad + (G_1 + 2G_2 - 2G_3)g(\xi_3(x_1,0),t)\\ &\quad + (G_1 - G_2 + G_3)g(\xi_4(x_1,0),t)\big\}\\ &\quad - \frac{1}{3}\big\{(G_1 - G_2 + G_3)g(\xi_5(x_1,0),t)\\ &\quad + (G_1 + 2G_2 - 2G_3)g(\xi_6(x_1,0),t)\\ &\quad + (G_1 - G_2 + G_3)g(\xi_7(x_1,0),t)\\ &\quad - 3G_1 g(\xi_8(x_1,0),t)\big\}\end{aligned} \tag{23}$$

$$\begin{aligned}\sigma_{2,T}(x_2, t) &\approx -\frac{1}{3}\big\{(G_1 - G_2 + G_3)g(\eta_1(x_2,0),t)\\ &\quad - (2G_1 + G_2 + 2G_3)g(\eta_2(x_2,0),t)\\ &\quad + (G_1 - G_2 + G_3) \times g(\eta_3(x_2,0),t)\\ &\quad + 3G_2 g(\eta_4(x_2,0),t)\\ &\quad - \frac{1}{3}\big\{3G_2 \times g(\eta_5(x_2,0),t)\\ &\quad + (G_1 - G_2 + G_3)g(\eta_6(x_2,0),t)\\ &\quad - (2G_1 + G_2 + 2G_3)g(\eta_7(x_2,0),t)\\ &\quad + (G_1 - G_2 + G_3)g(\eta_8(x_2,0),t)\big\}\end{aligned} \tag{24}$$

$$\begin{aligned}\sigma_{3,T}(x_3, t) &\approx -\frac{1}{3}\big\{-3G_3 g(\xi_1(x_3,0),t) + (G_1 - G_2 + G_3)\\ &\quad \times g(\xi_2(x_3,0),t)(-2G_1 + 2G_2 + G_3)g(\xi_3(x_3,0),t)\\ &\quad + (G_1 - G_2 + G_3)g(\xi_4(x_3,0),t)\big\}\\ &\quad - \frac{1}{3}\big\{(G_1 - G_2 + G_3) \times g(\xi_5(x_3,0),t)\\ &\quad + (-2G_1 + 2G_2 + G_3)g(\xi_6(x_3,0),t)\\ &\quad + (G_1 - G_2 + G_3)g(\xi_7(x_3,0),t)\\ &\quad - 3G_3 g(\xi_8(x_3,0),t)\big\}.\end{aligned} \tag{25}$$

The void nucleation time t_{nuc} can be obtained by solving the equations $\sigma_{1,T}(x_1, t_{\text{nuc},1}) = \sigma_{\text{crit}}$, $\sigma_{2,T}(x_2, t_{\text{nuc},2}) = \sigma_{\text{crit}}$, and $\sigma_{3,T}(x_3, t_{\text{nuc},3}) = \sigma_{\text{crit}}$. Fig. 6(a) demonstrates the stress distributions in the T-shaped tree shown in Fig. 5 that were obtained with COMSOL. Fig. 6(b) shows an evolution of the stress distributions along the segments 1 and 2 of the T-shaped tree that was obtained with COMSOL and the one-term approximation. Its comparison confirms that the one-term approximation is pretty accurate.

It should be noted that, in a case when the passive reservoir is present (dangling limb), then the corresponding continuity equation will have just stress gradient flux. For the upstream via (the test line is on a higher metal level compared to the current supply line) an ideal description should be modeled as a T-junction represented by a via-body (vertical segment) with the flux-divergence BC, a passive limb (left metal recess), and metal line on the right-hand side. The downstream via (test line is on a lower metal layer compared to the current supply line) can be represented just as a line edge with the flux-divergence BC.

C. Cross-Shaped Five-Terminal Interconnect Tree

In the cross-shaped five-terminal interconnect tree shown in Fig. 7 there are four segments which connect to each other through the middle node o. The exact analytical solution of

Authorized licensed use limited to: Univ of Calif Riverside. Downloaded on June 24,2026 at 15:12:23 UTC from IEEE Xplore. Restrictions apply.

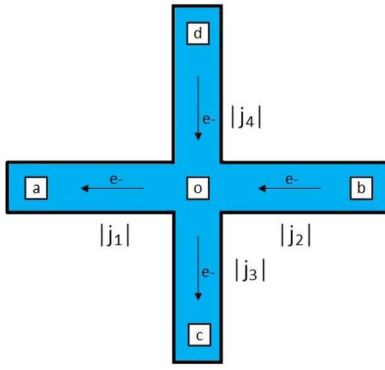

Fig. 7. Cross-shaped five-terminal interconnect tree.

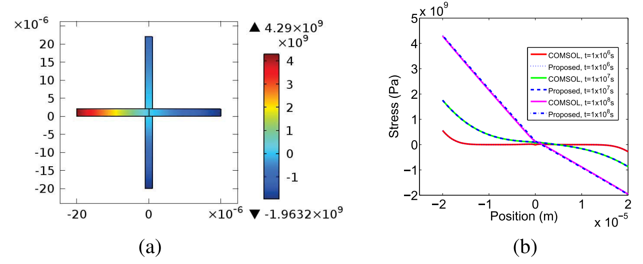

Fig. 8. (a) EM stress distribution in the cross-shaped four-terminal interconnect tree at the time $t = 1 \times 10^8$ s. (b) EM stress development along the lines 1 and 2: $j_1 = 4\times10^{10}$ A/m^2, $j_2 = 2\times10^{10}$ A/m^2, $j_3 = -2\times10^{10}$ A/m^2, and $j_4 = 1 \times 10^{10}$ A/m^2.

the stress evolution equation with the corresponding boundary and ICs can be obtained. The details for the mathematical derivation of the analytical EM analysis for this five-terminal interconnect tree can be found in the Appendix. Here we only show the final results.

Again, the approximate solution using the first slow-decaying dominant term for every branch in the cross-shaped tree provides

$$\begin{aligned}\sigma_{1,+}(x_1,t) &\approx -\frac{1}{4}\{-4G_1 g(\xi_1(x_1,0),t) + (G_1-G_2+G_3-G_4)\\ &\quad \times g(\xi_2(x_1,0),t) + 2(G_1+G_2-G_3+G_4)\\ &\quad \times g(\xi_3(x_1,0),t) + (G_1-G_2+G_3-G_4)\\ &\quad \times g(\xi_4(x_1,0),t)\}\\ &\quad -\frac{1}{4}\{(G_1-G_2+G_3-G_4)g(\xi_5(x_1,0),t)\\ &\quad + 2(G_1+G_2-G_3+G_4)\times g(\xi_6(x_1,0),t)\\ &\quad + (G_1-G_2+G_3-G_4)g(\xi_7(x_1,0),t)\\ &\quad - 4G_1 g(\xi_8(x_1,0),t)\} \end{aligned} \tag{26}$$

$$\begin{aligned}\sigma_{2,+}(x_2,t) &\approx -\frac{1}{4}\{(G_1-G_2+G_3-G_4)g(\eta_1(x_2,0),t)\\ &\quad - 2(G_1+G_2+G_3-G_4)g(\eta_2(x_2,0),t)\\ &\quad + (G_1-G_2+G_3-G_4)g(\eta_3(x_2,0),t)\\ &\quad + 4G_2 g(\eta_4(x_2,0),t)\}\\ &\quad -\frac{1}{4}\{4G_2\times g(\eta_5(x_2,0),t) + (G_1-G_2+G_3-G_4)\\ &\quad \times g(\eta_6(x_2,0),t)\\ &\quad - 2(G_1+G_2+G_3-G_4)g(\eta_7(x_2,0),t)\\ &\quad + (G_1-G_2+G_3-G_4)g(\eta_8(x_2,0),t)\} \end{aligned} \tag{27}$$

$$\begin{aligned}\sigma_{3,+}(x_3,t) &\approx -\frac{1}{4}\{-4G_3 g(\xi_1(x_3,0),t) + (G_1-G_2+G_3-G_4)\\ &\quad \times g(\xi_2(x_3,0),t) + 2(-G_1+G_2+G_3+G_4)\\ &\quad \times g(\xi_3(x_3,0),t) + (G_1-G_2+G_3-G_4)\\ &\quad \times g(\xi_4(x_3,0),t)\\ &\quad -\frac{1}{4}\{(G_1-G_2+G_3-G_4)g(\xi_5(x_3,0),t)\\ &\quad + 2(-G_1+G_2+G_3+G_4)g(\xi_6(x_3,0),t)\\ &\quad + (G_1-G_2+G_3-G_4)\times g(\xi_7(x_3,0),t)\\ &\quad - 4G_3 g(\xi_8(x_3,0),t)\} \end{aligned} \tag{28}$$

$$\begin{aligned}\sigma_{4,+}(x_4,t) &\approx -\frac{1}{4}\{(G_1-G_2+G_3-G_4)g(\eta_1(x_4,0),t)\\ &\quad - 2(G_1-G_2+G_3+G_4)g(\eta_2(x_4,0),t)\\ &\quad + (G_1-G_2+G_3-G_4)g(\eta_3(x_4,0),t)\\ &\quad + 4G_4 g(\eta_4(x_4,0),t)\\ &\quad -\frac{1}{4}\{4G_4\times g(\eta_5(x_4,0),t) + (G_1-G_2+G_3-G_4)\\ &\quad \times g(\eta_6(x_4,0),t) - 2(G_1-G_2+G_3+G_4)\\ &\quad \times g(\eta_7(x_4,0),t) + (G_1-G_2+G_3-G_4)\\ &\quad \times g(\eta_8(x_4,0),t). \end{aligned} \tag{29}$$

As before, we can calculate the void nucleation time t_{nuc} by solving the four equations $\sigma_{1,+}(x_1, t_{\text{nuc},1}) = \sigma_{\text{crit}}$, $\sigma_{2,+}(x_2, t_{\text{nuc},2}) = \sigma_{\text{crit}}$, $\sigma_{3,+}(x_3, t_{\text{nuc},3}) = \sigma_{\text{crit}}$, and $\sigma_{4,+}(x_4, t_{\text{nuc},4}) = \sigma_{\text{crit}}$.

As an illustration, we set the current densities in the four segments to $j_1 = 4 \times 10^{10}$ A/m^2, $j_2 = 2 \times 10^{10}$ A/m^2, $j_3 = -2 \times 10^{10} A/m^2 \times 10^{10}$ A/m^2, and $j_4 = 1 \times 10^{10}$ A/m^2. We use COMSOL to simulate the stress distributions in the cross-shaped tree shown in Fig. 8(a). Stress evolution obtained with our model using the one-term approximation fits well the simulation results obtained with COMSOL [Fig. 8(b)].

D. Interconnects With More Complex Structures

We have derived analytical models for EM reliability analysis in the straight-line three-terminal interconnect tree, the T-shaped four-terminal interconnect tree and the cross-shaped five-terminal interconnect tree, which reflect the practical VLSI interconnect architectures and interconnect layout-design techniques. The effects of temperature, current density, and segment length on stress evolution can be easily observed from the proposed analytical models. The developed methodology treats all involved current densities as the effective one. It means that the time-dependent currents are replaced by the effective DC currents, which are calculated on the basis of equal void nucleation times caused by these two currents [26].

In actual integrated circuits there are various types of interconnect trees as shown in Table II which shows EM-induced reliability models in various studies. Reliability analysis approaches for the straight-line three-terminal wires, the T-shaped four-terminal wires, and the cross-shaped five-terminal wires have also been presented in [17], [27] and [28]. Experimental characterization for the three-terminal interconnect tree has been investigated in [17]. A hierarchical reliability methodology for interconnects has been proposed in [27] to calculate time-to-failures which are combined using a joint

Authorized licensed use limited to: Univ of Calif Riverside. Downloaded on June 24,2026 at 15:12:23 UTC from IEEE Xplore. Restrictions apply.

TABLE II
EM RELIABILITY MODELS IN VARIOUS STUDIES

Ref.	Type of interconnects	Analytic model	Remarks
[11]	2-terminal	Available	EM of confined interconnect lines
[15]	3-terminal	NA	SEM characterization
[17]	3-terminal	NA	Experimental characterization
[19]	3-terminal	NA	L-shaped interconnect tree
[20]	Star-like	Available	Semi-infinite segments
[21]	Multi-terminal	NA	Nodal analysis for electromigration
[27]	Multi-terminal	NA	Hierarchical reliability methodology
[28]	Multi-terminal	NA	Experimental characterization
Proposed	Multi-terminal	Available	Multi-branch interconnect trees

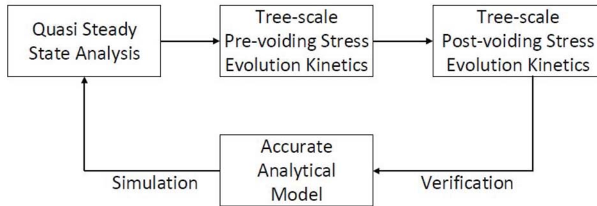

Fig. 9. EM-related reliability analysis flow based on the analytic model.

stochastic model of different trees. Experimental characterization of the reliability of Cu dual-damascene interconnect trees with three-terminal, four-terminal, and five-terminal configurations has been investigated in [28]. But they did not give a unified analytic form to calculate the stress evolution during the void nucleation phase for these interconnect trees.

It should be noted that while simulation of stress evolution in complex interconnect trees is possible, less computationally intensive analytical models are needed for calculating EM-induced stress evolution. As pointed out in [20], it is impossible to analyze and fabricate all the possible interconnect trees found in an integrated circuit. But we can develop a set of rules and specifications to make realistic reliability assessments of interconnects during the VLSI layout design process. The purpose of this paper is to obtain analytical models of EM-induced stress evolution in a multibranch tree by de-coupling the individual segments through the proper BC accounting the interactions between different branches. The proposed analytical models can also be applied for detailed calculation of the time-dependent stress analysis in the hierarchical reliability methodology for circuit level reliability analysis of interconnects.

In the practical IC design flow, for EM sign-off analysis, the accurate analysis of the stress evolution of multibranch interconnect trees are first performed for quasi steady state analysis which shows trees with the potential hydrostatic stress larger than the critical stress. Then the tree-scale prevoiding stress evolution kinetics (the technique proposed in this paper) provides an the exact location and the instance time for the first nucleated void. Then the post-voiding stress evolution kinetics combined with the adjusted current densities everywhere in the tree provides the locations and nucleation times for all other possible voids inside this tree. In the flowchart shown in Fig. 9, stress evolution kinetics analyses for multibranch interconnect trees are fed into accurate analytical models, such as the ones proposed in this paper.

This methodology, which was demonstrated on three different segment configurations, has a general character. It can be implemented in the trees where the "steady-state analysis" shows the locations with the stresses exceeding the critical stress. It will provide an accurate void nucleation time in each tree. These instances in time indicate when the resistances of individual segments start to evolve resulting the current density redistribution. These accurate nucleation times will be used in the EM assessment flow, described in [9], replacing the employed approximation-based nucleation times. The post-voiding stress evolution, which is under development now, will allow to predict generation of additional voids in the same interconnect tree, i.e., will lead to more accurate assessment of the evolution of the resistance of interconnect segments, and finally to accurate assessment of IR-drop degradation. As demonstrated in the Appendix, the initial problem of solution of the systems of PDEs reduces to solution of the sparse systems of linear algebraic equations. It can be done for any size of the problem. Thus, stress evolution inside interconnect tree of any size can be resolved with required efficiency and accuracy.

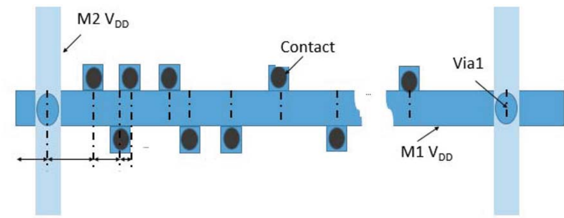

Fig. 10. Example of general realistic interconnect structure.

In order to further illustrate how the analytical model can be extended to a more complex structure, we show an individual interconnect tree of the power delivery grid, as shown in Fig. 10. It represents a long metal line with a number of the voltage ports, represented by the vias located at the intersections between power grids (p-g) of the neighboring metal levels, and a much larger number of the current ports, represented by the contacts connecting power grid with the circuits. The latter should be attributed mostly to the trees of the p-g located at the lowest metal level (M1). In general case the V_{DD} M1 power rail is characterized by presence of a large number of the upstream, regarding electron flow, tungsten contacts. V_{SS} rail is stuffed with the downstream tungsten contacts. Due to an extremely low atomic diffusivity of tungsten and, so, a big resistance to EM, the V_{DD} M1 power rail should be more susceptible to EM. Fig. 10 shows the schematics of the V_{DD} M1 power rail.

The V_{DD} rail should be divided on the set of segments with the ends represented the voltage and current ports and the ends of the rail. It should be mentioned that due to the very short lengths of the connections between the contact pads and the rail we do not account them in our set up. Stress evolution equations (1) written for each segment and coupled to each other by the BC representing the continuity of stress and fluxes at all junctions should be solved. The general system of equation in this case is a simple n-branch extension of the system (6) written for the case of two connected segments

$$\begin{aligned}
\frac{\partial \sigma_1}{\partial t} &= \frac{\partial}{\partial x}\left[\kappa_1\left(\frac{\partial \sigma_1}{\partial x}+G_1\right)\right],\ 0 \le x \le l_1 \\
\frac{\partial \sigma_2}{\partial t} &= \frac{\partial}{\partial x}\left[\kappa_2\left(\frac{\partial \sigma_2}{\partial x}+G_2\right)\right],\ l_1 \le x \le l_2 \\
&\cdots\cdots \\
\frac{\partial \sigma_{n-1}}{\partial t} &= \frac{\partial}{\partial x}\left[\kappa_{n-1}\left(\frac{\partial \sigma_{n-1}}{\partial x}+G_{n-1}\right)\right],\ l_{n-2} \le x \le l_{n-1} \\
\frac{\partial \sigma_n}{\partial t} &= \frac{\partial}{\partial x}\left[\kappa_n\left(\frac{\partial \sigma_n}{\partial x}+G_n\right)\right],\ l_{n-1} \le x \le L.
\end{aligned} \tag{30}$$

Authorized licensed use limited to: Univ of Calif Riverside. Downloaded on June 24,2026 at 15:12:23 UTC from IEEE Xplore. Restrictions apply.

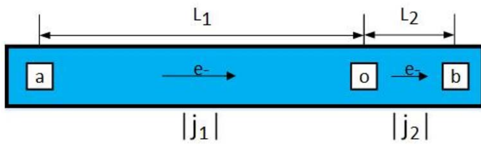

Fig. 11. Straight-line three-terminal interconnect tree with a variable segment length.

BC for these equations similarly to (7) are the follows:

$$\begin{aligned}
&\kappa_1\left(\frac{\partial\sigma_1}{\partial x}+G_1\right)=0,\ x=0\\
&\quad\sigma_1=\sigma_2,\ x=l_1\\
&\kappa_1\left(\frac{\partial\sigma_1}{\partial x}+G_1\right)=\kappa_2\left(\frac{\partial\sigma_2}{\partial x}+G_2\right),\ x=l_1\\
&\quad\sigma_2=\sigma_3,\ x=l_2\\
&\kappa_2\left(\frac{\partial\sigma_2}{\partial x}+G_2\right)=\kappa_3\left(\frac{\partial\sigma_3}{\partial x}+G_3\right),\ x=l_2\\
&\qquad\cdots\cdots\\
&\kappa_n\left(\frac{\partial\sigma_n}{\partial x}+G_n\right)=0,\ x=L.
\end{aligned}\tag{31}$$

ICs are: $\sigma_i = 0$ at $t = 0$ at all segments. After transforming all the equations and the corresponding BC into Laplace space we get a system of n equations similar to (9) and BC represented by $n + 1$ equations similar to (11). Solution of each ordinary differential equation represented by (10) with two unknown parameters, which will be found from BC, similarly to what was done in the case of two-segments/three terminals case, (13). A problem that we are solving is determination of the moment of time and location on the V_{DD} rail when and where the first void will be nucleated. To do this we do not need to make the inverse Laplace transformation. It is enough to compare the stress in the Laplace space $\sigma_i(x, s)$ with the Laplace transform of the critical stress. It should be also taken into account that not all junctions but just some of them can provide a condition for void nucleation: $\sigma = \sigma_{\text{crit}}$. Basically just two types of junctions characterized by specific configurations of the current directions should be considered. First type is the terminating segments serving as the current outlets (electron cathodes), and second the junctions separating two segments with electron flows directed outward this junctions.

IV. Effect of the Segment Length in EM-Induced Stress Evolution

By using the analytical method proposed in Section III, we can obtain closed-form expressions for the EM-induced stress evolution in multibranch interconnect trees with a variable segment length. This is demonstrated by investigating the effect of segment length on the stress evolution in the straight-line three-terminal interconnect tree shown in Fig. 11.

Results of the performed analysis are shown in Fig. 12(a)–(d). The directions of the currents in the segments are chosen to be opposite to each other, which causes the tensile stress development at both cathode ends "a" and "b." The stress evolution is analyzed with the proposed analytical method. They demonstrate that the decreasing of the length of one of the segments taking place under the fixed electric current load results a progressive development of the compressive stress in this segment. This is caused by a continuously increasing back stress gradient in the short segment due to a continuous supply of atoms from the long segment to the segment boarder. On the other hand, as seen in Fig. 12(c) and (d), a tensile stress can also build up in the right segment if the length of this segment is long enough. By varying the values of the applied current and the segment length one can reach the situation when a void is nucleated first in the short segment.

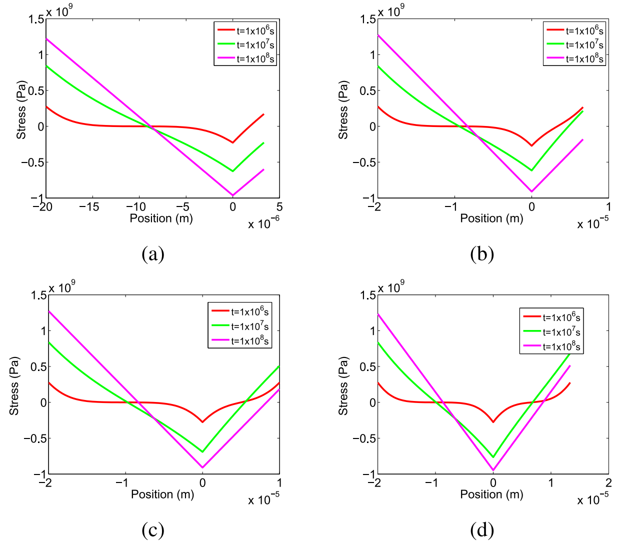

Fig. 12. EM stress development along the segments 1 and 2 in the three-terminal interconnect tree. (a) $L_2 = (1/6)L_1$. (b) $L_2 = (2/6)L_1$. (c) $L_2 = (3/6)L_1$. (d) $L_2 = (4/6)L_1$. For call cases: $j_1 = 2 \times 10^{10}$ A/m^2 and $j_2 = -2 \times 10^{10}$ A/m^2.

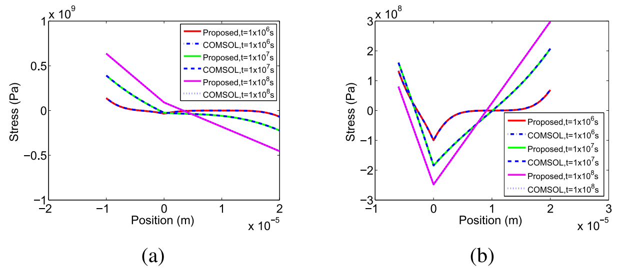

Fig. 13. EM stress development along the segments 1 and 2 in the three-terminal interconnect tree. (a) $j_1 = 1 \times 10^{10}$ A/m^2, $j_2 = 5 \times 10^9$ A/m^2, $L_1 = 10\ \mu$m, and $L_2 = 20\ \mu$m. (b) $j_1 = 1 \times 10^{10}$ A/m^2, $j_2 = -5 \times 10^9$ A/m^2, $L_1 = 6\ \mu$m, and $L_2 = 20\ \mu$m.

The stress profiles for different times shown in Fig. 13 are obtained from the proposed analytical method and COMSOL simulation. It can be seen from Fig. 13 that the proposed analytical method fits well to the results of the numerical simulations at every time instance. Experimental results show that the proposed analytical method generates very small errors, which is sufficient for practical EM analysis.

V. Experimental Results and Discussion

The proposed dynamic EM model and the method of analysis of multibranch interconnect trees have been implemented in MATLAB and compared with COMSOL, which is considered as a "golden" tool in this paper. The material parameters used in our numerical simulations are shown in Table I. Different trees used in our experiment are shown in Figs. 3, 5, and 7. The length of each segment was set to 20 μm.

Authorized licensed use limited to: Univ of Calif Riverside. Downloaded on June 24,2026 at 15:12:23 UTC from IEEE Xplore. Restrictions apply.

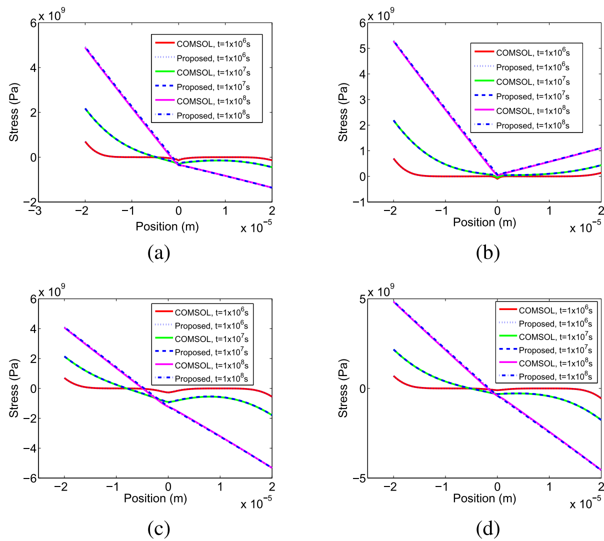

Fig. 14. EM stress development along the lines 1 and 2 in the cross-shaped five-terminal interconnect tree. (a) $j_1 = 5 \times 10^{10}$ A/m^2, $j_2 = 1 \times 10^{10}$ A/m^2, $j_3 = 2.5 \times 10^{10}$ A/m^2, and $j_4 = 4 \times 10^{10}$ A/m^2. (b) $j_1 = 5 \times 10^{10}$ A/m^2, $j_2 = -1 \times 10^{10}$ A/m^2, $j_3 = -2.5 \times 10^{10}$ A/m^2, and $j_4 = 4 \times 10^{10}$ A/m^2. (c) $j_1 = 5 \times 10^{10}$ A/m^2, $j_2 = 4 \times 10^{10}$ A/m^2, $j_3 = 3 \times 10^{10}$ A/m^2, and $j_4 = -5 \times 10^{10}$ A/m^2. (d) $j_1 = 5 \times 10^{10}$ A/m^2, $j_2 = 4 \times 10^{10}$ A/m^2, $j_3 = -3 \times 10^{10}$ A/m^2, and $j_4 = -5 \times 10^{10}$ A/m^2.

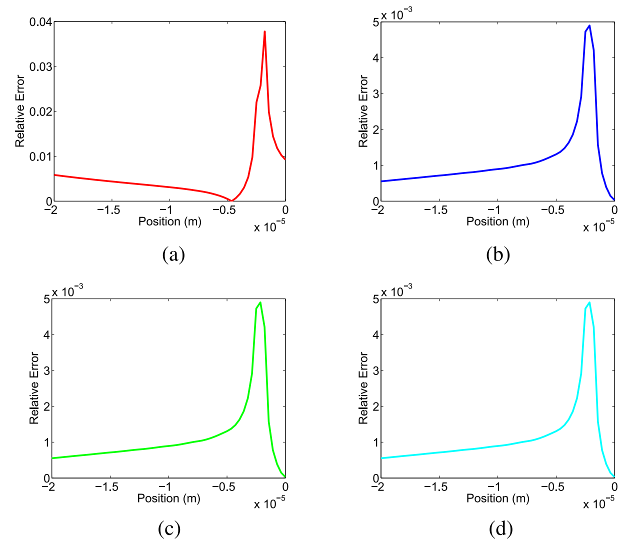

Fig. 15. Relative errors between the proposed analytical model and the COMSOL model for the straight-line three-terminal interconnect tree: $j_1 = 5 \times 10^{10}$ A/m^2 and $j_2 = 3 \times 10^{10}$ A/m^2. Relative errors using (a) one item, (b) two items, (c) five items, and (d) ten items.

A. EM Model Predictions With Different Current Densities

First, we analyze the EM model predictions against the results of COMSOL simulations using the one term approximation for the cross-shaped five-terminal interconnect tree. The numerical results for the T-shaped four-terminal interconnect tree have been discussed in [29]. The EM induced stress distributions of the cross-shaped wire structure (here the only segments 1 and 2 are shown) under different current density sets are shown in Fig. 14(a)–(d). The stress profiles for different times are obtained from the one term approximation of the exact series solution. In the case (a), the stress distribution is similar to the three-terminal single-wire case where the segment 1 (left) is the reservoir and the segment 2 (right) is the active sink with small current. Since $j_1 \gg j_2$, the hydrostatic stress in the segment 2 are all compressive (negative). For the case (b), the currents in these segments have different directions. As a result, both of the segments demonstrate tensile stresses, which matches well the results obtained with COMSOL.

B. Accuracy Study for the Compact EM Models

Next, we study the accuracy of the EM models employing different number of terms in the exact solution against the COMSOL. Due to limited space, we only show the results for the straight-line three-terminal interconnect case. We plot the relative errors against COMSOL results for the cases using one term ($n = 0$), two terms ($n = 1$), five terms ($n = 4$), and ten terms ($n = 9$), which are shown in Fig. 15(a)–(d), respectively. As we can see, by using just one term ($n = 0$), we can obtain relative errors less than 4%. By using two terms ($n = 1$), the error is reduced to 0.5%. By using more terms ($n = 4$ and $n = 9$), the errors will still stay around 0.5%, which means that two terms can achieve sufficient accuracy and adding more terms does not increase the accuracy significantly. This is also valid for all other considered interconnect trees.

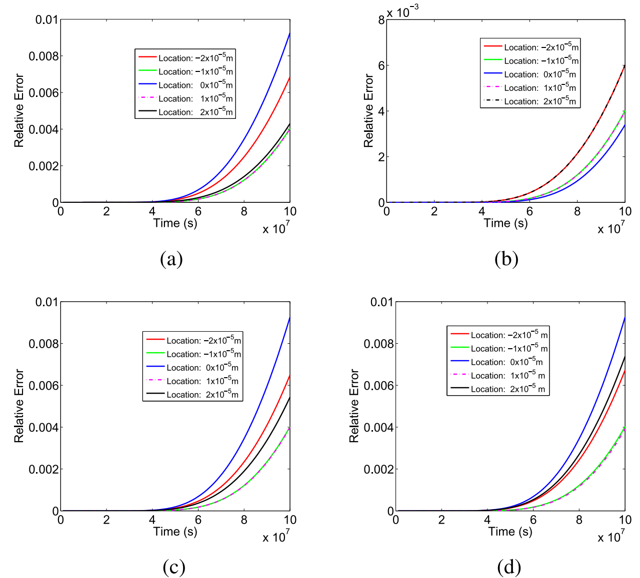

Fig. 16. Relative errors between the one-term and two-term approximations for the cross-shaped five-terminal wires. (a) $j_1 = 5 \times 10^{10}$ A/m^2, $j_2 = 10^{10}$ A/m^2, $j_3 = 5 \times 10^{10}$ A/m^2, and $j_4 = 10^{10}$ A/m^2. (b) $j_1 = 5 \times 10^{10}$ A/m^2, $j_2 = -10^{10}$ A/m^2, $j_3 = -5 \times 10^{10}$ A/m^2, and $j_4 = 10^{10}$ A/m^2. (c) $j_1 = 5 \times 10^{10}$ A/m^2, $j_2 = 3 \times 10^{10}$ A/m^2, $j_3 = 2 \times 10^{10}$ A/m^2, and $j_4 = -10^{10}$ A/m^2. (d) $j_1 = 5 \times 10^{10}$ A/m^2, $j_2 = -3 \times 10^{10}$ A/m^2, $j_3 = -2 \times 10^{10}$ A/m^2, and $j_4 = -10^{10}$ A/m^2.

C. Convergence Analysis of the Infinite-Series Solution

To analyze the convergence behavior of the infinite-series solution obtained by the aforementioned method, we need to compare the $(m + l)$-term approximation with the m-term approximation for arbitrary fixed non-negative integers m and l. Fig. 15(a) illustrates that there are only a few locations in the metal wire where the relative errors stay around 4%. We obtain similar results, when the one-term approximation is applied, for the T-shaped four-terminal and cross-shaped five-terminal interconnect trees. It can been observed from Fig. 15(b) that the relative errors using the

Authorized licensed use limited to: Univ of Calif Riverside. Downloaded on June 24,2026 at 15:12:23 UTC from IEEE Xplore. Restrictions apply.

$$\begin{bmatrix} \frac{a_1}{d_1} & -a_1 d_1 & 0 & 0 & 0 & 0 \\ 0 & 0 & a_2 d_2 & -\frac{a_2}{d_2} & 0 & 0 \\ 0 & 0 & 0 & 0 & \frac{a_3}{d_3} & -a_3 d_3 \\ \kappa_1 a_1 & -\kappa_1 a_1 & -\kappa_2 a_2 & \kappa_2 a_2 & \kappa_3 a_3 & -\kappa_3 a_3 \\ 1 & 1 & -1 & -1 & 0 & 0 \\ 0 & 0 & 1 & 1 & -1 & -1 \end{bmatrix} \begin{bmatrix} A_{1,T} \\ B_{1,T} \\ A_{2,T} \\ B_{2,T} \\ A_{3,T} \\ B_{3,T} \end{bmatrix} = \begin{bmatrix} -c_1 \\ -c_2 \\ -c_3 \\ -\kappa_1 c_1 + \kappa_2 c_2 - \kappa_3 c_3 \\ 0 \\ 0 \end{bmatrix} \quad (33)$$

$$\begin{aligned} A_{1,T} &= \left\{3c_1 d^{-3} - (c_1 - c_2 + c_3)d^{-2} - (c_1 + 2c_2 - 2c_3)d^{-1} - (c_1 - c_2 + c_3)\right\} \Big/ \left\{3a\left(1 - d^{-4}\right)\right\} \\ B_{1,T} &= \left\{-(c_1 - c_2 + c_3)d^{-4} - (c_1 + 2c_2 - 2c_3)d^{-3} - (c_1 - c_2 + c_3)d^{-2} + 3c_1 d^{-1}\right\} \Big/ \left\{3a\left(1 - d^{-4}\right)\right\} \\ A_{2,T} &= \left\{-(c_1 - c_2 + c_3)d^{-4} + (2c_1 + c_2 + 2c_3)d^{-3} - (c_1 - c_2 + c_3)d^{-2} - 3c_2 d^{-1}\right\} \Big/ \left\{3a\left(1 - d^{-4}\right)\right\} \\ B_{2,T} &= \left\{-3c_2 d^{-3} - (c_1 - c_2 + c_3)d^{-2} + (2c_1 + c_2 + 2c_3)d^{-1} - (c_1 - c_2 + c_3)\right\} \Big/ \left\{3a\left(1 - d^{-4}\right)\right\} \\ A_{3,T} &= \left\{3c_3 d^{-3} - (c_1 - c_2 + c_3)d^{-2} - (-2c_1 + 2c_2 + c_3)d^{-1} - (c_1 - c_2 + c_3)\right\} \Big/ \left\{3a\left(1 - d^{-4}\right)\right\} \\ B_{3,T} &= \left\{-(c_1 - c_2 + c_3)d^{-4} - (-2c_1 + 2c_2 + c_3)d^{-3} - (c_1 - c_2 + c_3)d^{-2} + 3c_3 d^{-1}\right\} \Big/ \left\{3a\left(1 - d^{-4}\right)\right\} \end{aligned} \quad (34)$$

two-term approximation are just about 0.5%. Therefore, for discussing the convergence behavior of the infinite-series solution to the stress evolution in EM reliability analysis, we turn out to compare the one-term approximation with the two-term approximation. This comparison can be seen easily from the numerical simulation results. Fig. 16 shows the comparison results between the one-term and two-term approximations for the cross-shaped five-terminal interconnect tree. We can see from Fig. 16 that the relative errors between the one-term and two-term approximations are less than 1%, which shows that the dominant one-term approximation is sufficient for practical EM analysis.

VI. Conclusion

In this paper, we have proposed a new modeling and analysis technique for EM reliability analysis in multibranch interconnect trees, which are common for practical VLSI interconnect architectures and wiring techniques. We have derived the exact analytical solutions to the stress evolution equations for the straight-line three-terminal wires, the T-shaped four-terminal wires, and the cross-shaped five-terminal wires. The new physics-based EM models for multibranch interconnect trees show an excellent agreement with the detailed numerical analysis. Experimental results showed that using the first dominant basis function can lead to less than 4% errors. Furthermore, by using the first two basis functions, one can have less than 0.5% errors, which is sufficient for practical EM analysis.

Appendix

In this section, we list details for the mathematical derivation of our analytical EM analysis for the T-shaped four-terminal interconnect tree and the cross-shaped five-terminal interconnect tree.

A. Complete Solutions for the T-Shaped Four-Terminal Interconnect Tree

The stress evolution equations for an interconnect tree consisting of three segments

$$\begin{aligned} \frac{\partial \sigma_1}{\partial t} &= \frac{\partial}{\partial x_1}\left[\kappa_1\left(\frac{\partial \sigma_1}{\partial x_1} + G_1\right)\right], -L < x_1 < 0,\ t > 0 \\ \frac{\partial \sigma_2}{\partial t} &= \frac{\partial}{\partial x_2}\left[\kappa_2\left(\frac{\partial \sigma_2}{\partial x_2} + G_2\right)\right], 0 < x_2 < L,\ t > 0 \\ \frac{\partial \sigma_3}{\partial t} &= \frac{\partial}{\partial x_3}\left[\kappa_3\left(\frac{\partial \sigma_3}{\partial x_3} + G_3\right)\right], -L < x_3 < 0,\ t > 0 \end{aligned}$$

subject to the BCs

$$\begin{aligned} &\kappa_1\left(\frac{\partial \sigma_1}{\partial x_1} + G_1\right) = 0, \quad x_1 = -L,\ t > 0 \\ &\sigma_1 = \sigma_2 = \sigma_3,\ x_1 = x_2 = x_3 = 0,\ t > 0 \\ &\kappa_1\left(\frac{\partial \sigma_1}{\partial x_1} + G_1\right) - \kappa_2\left(\frac{\partial \sigma_2}{\partial x_2} + G_2\right) \\ &\qquad + \kappa_3\left(\frac{\partial \sigma_3}{\partial x_3} + G_3\right) = 0,\ x_1 = x_2 = x_3 = 0,\ t > 0 \\ &\kappa_2\left(\frac{\partial \sigma_2}{\partial x_2} + G_2\right) = 0, \quad x_2 = L,\ t > 0 \\ &\kappa_3\left(\frac{\partial \sigma_3}{\partial x_3} + G_3\right) = 0, \quad x_3 = -L,\ t > 0 \end{aligned}$$

and the ICs

$$\begin{aligned} \sigma_1(x_1, t) &= 0, \quad -L < x_1 < 0,\ t = 0 \\ \sigma_2(x_2, t) &= 0, \quad 0 < x_2 < L,\ t = 0 \\ \sigma_3(x_3, t) &= 0, \quad -L < x_3 < 0,\ t = 0. \end{aligned}$$

We use the Laplace transform technique to solve the stress evolution equation with given BC and IC for the T-shaped four-terminal interconnect tree. By applying the Laplace transform, the analytical solutions in s-domain for each branch can be given as

$$\begin{aligned} \hat{\sigma}_1(x, s) &= A_{1,T} e^{\sqrt{\frac{s}{\kappa_1}}x} + B_{1,T} e^{-\sqrt{\frac{s}{\kappa_1}}x} \\ \hat{\sigma}_2(x, s) &= A_{2,T} e^{\sqrt{\frac{s}{\kappa_2}}x} + B_{2,T} e^{-\sqrt{\frac{s}{\kappa_2}}x} \\ \hat{\sigma}_3(x, s) &= A_{3,T} e^{\sqrt{\frac{s}{\kappa_3}}x} + B_{3,T} e^{-\sqrt{\frac{s}{\kappa_3}}x} \end{aligned} \quad (32)$$

where the coefficients $A_{i,T}$ and $B_{i,T} (i = 1, 2, 3)$ satisfy the linear system (33) (shown at the top of this page). Assuming that $\kappa_1 = \kappa_2 = \kappa_3 = \kappa$, then we have $a_1 = a_2 = a_3 = a$, $b_1 = b_2 = b_3 = b$, and $d_1 = d_2 = d_3 = d$. With this assumption, the coefficients $A_{i,T}$ and $B_{i,T}$ can be calculated by (34) (shown at the top of this page). By applying the inverse

Authorized licensed use limited to: Univ of Calif Riverside. Downloaded on June 24,2026 at 15:12:23 UTC from IEEE Xplore. Restrictions apply.

Laplace transformation to $\hat{\sigma}_i(x, s)$ in (32), we can obtain an exact time domain solution

$$\begin{aligned}
&\sigma_{1,T}(x_1, t)\\
&= -\frac{1}{3}\sum_{n=0}^{+\infty}\Big\{-3G_1 g(\xi_1(x_1, n), t) + (G_1 - G_2 + G_3)\\
&\quad \times g(\xi_2(x_1, n), t) + (G_1 + 2G_2 - 2G_3)\\
&\quad \times g(\xi_3(x_1, n), t) + (G_1 - G_2 + G_3)\\
&\quad \times g(\xi_4(x_1, n), t)\Big\}\\
&\quad - \frac{1}{3}\sum_{n=0}^{+\infty}\Big\{(G_1 - G_2 + G_3)g(\xi_5(x_1, n), t)\\
&\quad + (G_1 + 2G_2 - 2G_3)g(\xi_6(x_1, n), t)\\
&\quad + (G_1 - G_2 + G_3)g(\xi_7(x_1, n), t)\\
&\quad - 3G_1 g(\xi_8(x_1, n), t)\Big\}\\
&\sigma_{2,T}(x_2, t)\\
&= -\frac{1}{3}\sum_{n=0}^{+\infty}\Big\{(G_1 - G_2 + G_3)g(\eta_1(x_2, n), t)\\
&\quad - (2G_1 + G_2 + 2G_3)g(\eta_2(x_2, n), t)\\
&\quad + (G_1 - G_2 + G_3) \times g(\eta_3(x_2, n), t)\\
&\quad + 3G_2 g(\eta_4(x_2, n), t)\\
&\quad - \frac{1}{3}\sum_{n=0}^{+\infty}\Big\{3G_2 \times g(\eta_5(x_2, n), t) + (G_1 - G_2 + G_3)\\
&\quad \times g(\eta_6(x_2, n), t) - (2G_1 + G_2 + 2G_3)\\
&\quad \times g(\eta_7(x_2, n), t) + (G_1 - G_2 + G_3)\\
&\quad \times g(\eta_8(x_2, n), t)\Big\}\\
&\sigma_{3,T}(x_3, t)\\
&= -\frac{1}{3}\sum_{n=0}^{+\infty}\Big\{-3G_3 g(\xi_1(x_3, n), t) + (G_1 - G_2 + G_3)\\
&\quad \times g(\xi_2(x_3, n), t)(-2G_1 + 2G_2 + G_3)\\
&\quad \times g(\xi_3(x_3, n), t) + (G_1 - G_2 + G_3)\\
&\quad \times g(\xi_4(x_3, n), t)\Big\}\\
&\quad - \frac{1}{3}\sum_{n=0}^{+\infty}\Big\{(G_1 - G_2 + G_3) \times g(\xi_5(x_3, n), t)\\
&\quad + (-2G_1 + 2G_2 + G_3)g(\xi_6(x_3, n), t)\\
&\quad + (G_1 - G_2 + G_3)g(\xi_7(x_3, n), t)\\
&\quad - 3G_3 g(\xi_8(x_3, n), t)\Big\}.
\end{aligned}$$

B. Complete Solutions for the Cross-Shaped Five-Terminal Interconnect Tree

The stress evolution equations for an interconnect tree consisting of four segments

$$\begin{aligned}
\frac{\partial\sigma_1}{\partial t} &= \frac{\partial}{\partial x_1}\left[\kappa_1\left(\frac{\partial\sigma_1}{\partial x_1} + G_1\right)\right],\ -L < x_1 < 0,\ t > 0\\
\frac{\partial\sigma_2}{\partial t} &= \frac{\partial}{\partial x_2}\left[\kappa_2\left(\frac{\partial\sigma_2}{\partial x_2} + G_2\right)\right],\ 0 < x_2 < L,\ t > 0\\
\frac{\partial\sigma_3}{\partial t} &= \frac{\partial}{\partial x_3}\left[\kappa_3\left(\frac{\partial\sigma_3}{\partial x_3} + G_3\right)\right],\ -L < x_3 < 0,\ t > 0\\
\frac{\partial\sigma_4}{\partial t} &= \frac{\partial}{\partial x_4}\left[\kappa_4\left(\frac{\partial\sigma_4}{\partial x_4} + G_4\right)\right],\ 0 < x_4 < L,\ t > 0
\end{aligned}$$

subject to the BCs

$$\begin{aligned}
&\kappa_1\left(\frac{\partial\sigma_1}{\partial x_1} + G_1\right) = 0,\quad x_1 = -L,\ t > 0\\
&\sigma_1 = \sigma_2 = \sigma_3 = \sigma_4,\ x_1 = x_2 = x_3 = x_4 = 0,\ t > 0\\
&\kappa_1\left(\frac{\partial\sigma_1}{\partial x_1} + G_1\right) - \kappa_2\left(\frac{\partial\sigma_2}{\partial x} + G_2\right)\\
&\qquad + \kappa_3\left(\frac{\partial\sigma_3}{\partial x_3} + G_3\right) - \kappa_4\left(\frac{\partial\sigma_4}{\partial x_4} + G_4\right) = 0,\\
&\qquad x_1 = x_2 = x_3 = x_4 = 0,\ t > 0\\
&\kappa_2\left(\frac{\partial\sigma_2}{\partial x_2} + G_2\right) = 0,\quad x_2 = L,\ t > 0\\
&\kappa_3\left(\frac{\partial\sigma_3}{\partial x_3} + G_3\right) = 0,\quad x_3 = -L,\ t > 0\\
&\kappa_4\left(\frac{\partial\sigma_4}{\partial x_4} + G_4\right) = 0,\quad x_2 = L,\ t > 0
\end{aligned}$$

and the ICs

$$\begin{aligned}
&\sigma_1(x_1, t) = 0,\quad -L < x_1 < 0,\ t = 0\\
&\sigma_2(x_2, t) = 0,\quad 0 < x_2 < L,\ t = 0\\
&\sigma_3(x_3, t) = 0,\quad -L < x_3 < 0,\ t = 0\\
&\sigma_4(x_4, t) = 0,\quad 0 < x_4 < L,\ t = 0.
\end{aligned}$$

By using the Laplace transform technique, we obtain an exact analytical solution in s-domain

$$\begin{aligned}
\hat{\sigma}_1(x, s) &= A_{1,+}e^{\sqrt{\frac{s}{\kappa_1}}x} + B_{1,+}e^{-\sqrt{\frac{s}{\kappa_1}}x}\\
\hat{\sigma}_2(x, s) &= A_{2,+}e^{\sqrt{\frac{s}{\kappa_2}}x} + B_{2,+}e^{-\sqrt{\frac{s}{\kappa_2}}x}\\
\hat{\sigma}_3(x, s) &= A_{3,+}e^{\sqrt{\frac{s}{\kappa_3}}x} + B_{3,+}e^{-\sqrt{\frac{s}{\kappa_3}}x}\\
\hat{\sigma}_4(x, s) &= A_{4,+}e^{\sqrt{\frac{s}{\kappa_4}}x} + B_{4,+}e^{-\sqrt{\frac{s}{\kappa_4}}x}
\end{aligned}\tag{37}$$

where the coefficients $A_{i,+}$ and $B_{i,+} (i = 1, 2, 3, 4)$ can be calculated by solving the linear system (35) (shown at the top of the next page). Assuming that $\kappa_1 = \kappa_2 = \kappa_3 = \kappa_4 = \kappa$, we have $a_1 = a_2 = a_3 = a$, $b_1 = b_2 = b_3 = b$, and $d_1 = d_2 = d_3 = d$. Thus, the coefficients $A_{i,+}$ and $B_{i,+}$ can be given by (36) (shown at the top of the next page). By using the inverse Laplace transform technique, we obtain

$$\begin{aligned}
&\sigma_{1,+}(x_1, t)\\
&= -\frac{1}{4}\sum_{n=0}^{+\infty}\Big\{-4G_1 g(\xi_1(x_1, n), t) + (G_1 - G_2 + G_3 - G_4)\\
&\quad \times g(\xi_2(x_1, n), t) + 2(G_1 + G_2 - G_3 + G_4)\\
&\quad \times g(\xi_3(x_1, n), t) + (G_1 - G_2 + G_3 - G_4)\\
&\quad \times g(\xi_4(x_1, n), t)\Big\}\\
&\quad - \frac{1}{4}\sum_{n=0}^{+\infty}\Big\{(G_1 - G_2 + G_3 - G_4)g(\xi_5(x_1, n), t)\\
&\quad + 2(G_1 + G_2 - G_3 + G_4) \times g(\xi_6(x_1, n), t)\\
&\quad + (G_1 - G_2 + G_3 - G_4)g(\xi_7(x_1, n), t)\\
&\quad - 4G_1 g(\xi_8(x_1, n), t)\Big\}
\end{aligned}$$

Authorized licensed use limited to: Univ of Calif Riverside. Downloaded on June 24,2026 at 15:12:23 UTC from IEEE Xplore. Restrictions apply.

$$\begin{bmatrix} \frac{a_1}{d_1} & -a_1d_1 & 0 & 0 & 0 & 0 & 0 & 0 \\ 0 & 0 & a_2d_2 & -\frac{a_2}{d_2} & 0 & 0 & 0 & 0 \\ 0 & 0 & 0 & 0 & \frac{a_3}{d_3} & -a_3d_3 & 0 & 0 \\ 0 & 0 & 0 & 0 & 0 & 0 & a_4d_4 & -\frac{a_4}{d_4} \\ \kappa_1a_1 & -\kappa_1a_1 & -\kappa_2a_2 & \kappa_2a_2 & \kappa_3a_3 & -\kappa_3a_3 & -\kappa_4a_4 & \kappa_4a_4 \\ 1 & 1 & -1 & -1 & 0 & 0 & 0 & 0 \\ 0 & 0 & 1 & 1 & -1 & -1 & 0 & 0 \\ 0 & 0 & 0 & 0 & 1 & 1 & -1 & -1 \end{bmatrix} \begin{bmatrix} A_{1,+} \\ B_{1,+} \\ A_{2,+} \\ B_{2,+} \\ A_{3,+} \\ B_{3,+} \\ A_{4,+} \\ B_{4,+} \end{bmatrix} = \begin{bmatrix} -c_1 \\ -c_2 \\ -c_3 \\ -c_4 \\ -\kappa_1c_1 + \kappa_2c_2 - \kappa_3c_3 + \kappa_4c_4 \\ 0 \\ 0 \\ 0 \end{bmatrix} \tag{35}$$

$$\begin{aligned}
A_{1,+} &= \left\{4c_1d^{-3} - (c_1 - c_2 + c_3 - c_4)d^{-2} - (2c_1 + 2c_2 - 2c_3 + 2c_4)d^{-1} - (c_1 - c_2 + c_3 - c_4)\right\} \Big/ \left\{4a\left(1 - d^{-4}\right)\right\} \\
B_{1,+} &= \left\{-(c_1 - c_2 + c_3 - c_4)d^{-4} - (2c_1 + 2c_2 - 2c_3 + 2c_4)d^{-3} - (c_1 - c_2 + c_3 - c_4)d^{-2} + 4c_1d^{-1}\right\} \Big/ \left\{4a\left(1 - d^{-4}\right)\right\} \\
A_{2,+} &= \left\{-(c_1 - c_2 + c_3 - c_4)d^{-4} + (2c_1 + 2c_2 + 2c_3 - 2c_4)d^{-3} - (c_1 - c_2 + c_3 - c_4)d^{-2} - 4c_2d^{-1}\right\} \Big/ \left\{4a\left(1 - d^{-4}\right)\right\} \\
B_{2,+} &= \left\{-4c_2d^{-3} - (c_1 - c_2 + c_3 - c_4)d^{-2} + (2c_1 + 2c_2 + 2c_3 - 2c_4)d^{-1} - (c_1 - c_2 + c_3 - c_4)\right\} \Big/ 4a\left(1 - d^{-4}\right) \\
A_{3,+} &= \left\{4c_3d^{-3} - (c_1 - c_2 + c_3 - c_4)d^{-2} - (-2c_1 + 2c_2 + 2c_3 + 2c_4)d^{-1} - (c_1 - c_2 + c_3 - c_4)\right\} \Big/ \left\{4a\left(1 - d^{-4}\right)\right\} \\
B_{3,+} &= \left\{-(c_1 - c_2 + c_3 - c_4)d^{-4} - (-2c_1 + 2c_2 + 2c_3 + 2c_4)d^{-3} - (c_1 - c_2 + c_3 - c_4)d^{-2} + 4c_3d^{-1}\right\} \Big/ \left\{4a\left(1 - d^{-4}\right)\right\} \\
A_{4,+} &= \left\{-(c_1 - c_2 + c_3 - c_4)d^{-4} + (2c_1 - 2c_2 + 2c_3 + 2c_4)d^{-3} - (c_1 - c_2 + c_3 - c_4)d^{-2} - 4c_4d^{-1}\right\} \Big/ \left\{4a\left(1 - d^{-4}\right)\right\} \\
B_{4,+} &= \left\{-4c_4d^{-3} - (c_1 - c_2 + c_3 - c_4)d^{-2} + (2c_1 - 2c_2 + 2c_3 + 2c_4)d^{-1} - (c_1 - c_2 + c_3 - c_4)\right\} \Big/ \left\{4a\left(1 - d^{-4}\right)\right\}
\end{aligned} \tag{36}$$

$$\begin{aligned}
&\sigma_{2,+}(x_2, t) \\
&= -\frac{1}{4}\sum_{n=0}^{+\infty}\Big\{(G_1 - G_2 + G_3 - G_4)g(\eta_1(x_2, n), t) \\
&\quad - 2(G_1 + G_2 + G_3 - G_4)g(\eta_2(x_2, n), t) \\
&\quad + (G_1 - G_2 + G_3 - G_4)g(\eta_3(x_2, n), t) \\
&\quad + 4G_2g(\eta_4(x_2, n), t)\Big\} \\
&\quad -\frac{1}{4}\sum_{n=0}^{+\infty}\Big\{4G_2 \times g(\eta_5(x_2, n), t) + (G_1 - G_2 + G_3 - G_4) \\
&\quad \times g(\eta_6(x_2, n), t) - 2(G_1 + G_2 + G_3 - G_4) \\
&\quad \times g(\eta_7(x_2, n), t) + (G_1 - G_2 + G_3 - G_4) \\
&\quad \times g(\eta_8(x_2, n), t)\Big\}
\end{aligned}$$

$$\begin{aligned}
&\sigma_{3,+}(x_3, t) \\
&= -\frac{1}{4}\sum_{n=0}^{+\infty}\Big\{-4G_3g(\xi_1(x_3, n), t) + (G_1 - G_2 + G_3 - G_4) \\
&\quad \times g(\xi_2(x_3, n), t) + 2(-G_1 + G_2 + G_3 + G_4) \\
&\quad \times g(\xi_3(x_3, n), t) + (G_1 - G_2 + G_3 - G_4) \\
&\quad \times g(\xi_4(x_3, n), t) \\
&\quad -\frac{1}{4}\sum_{n=0}^{+\infty}\Big\{(G_1 - G_2 + G_3 - G_4)g(\xi_5(x_3, n), t) \\
&\quad + 2(-G_1 + G_2 + G_3 + G_4)g(\xi_6(x_3, n), t) \\
&\quad + (G_1 - G_2 + G_3 - G_4) \times g(\xi_7(x_3, n), t) \\
&\quad - 4G_3g(\xi_8(x_3, n), t)\Big\}
\end{aligned}$$

$$\begin{aligned}
&\sigma_{4,+}(x_4, t) \\
&= -\frac{1}{4}\sum_{n=0}^{+\infty}\Big\{(G_1 - G_2 + G_3 - G_4)g(\eta_1(x_4, n), t) \\
&\quad - 2(G_1 - G_2 + G_3 + G_4)g(\eta_2(x_4, n), t) \\
&\quad + (G_1 - G_2 + G_3 - G_4)g(\eta_3(x_4, n), t) \\
&\quad + 4G_4g(\eta_4(x_4, n), t) \\
&\quad -\frac{1}{4}\sum_{n=0}^{+\infty}\Big\{4G_4 \times g(\eta_5(x_4, n), t) + (G_1 - G_2 + G_3 - G_4) \\
&\quad \times g(\eta_6(x_4, n), t) - 2(G_1 - G_2 + G_3 + G_4) \\
&\quad \times g(\eta_7(x_4, n), t) + (G_1 - G_2 + G_3 - G_4) \\
&\quad \times g(\eta_8(x_4, n), t).
\end{aligned}$$

REFERENCES

[1] B. Bailey, "Thermally challenged," *Semicond. Eng.*, Dec. 2013. [Online]. Available: http://semiengineering.com/thermally-challenged/, accessed Feb. 16, 2014.

[2] S. Chatterjee, M. B. Fawaz, and F. N. Najm, "Redundancy-aware electromigration checking for mesh power grids," in *Proc. IEEE/ACM Int. Conf. Comput.-Aided Design (ICCAD)*, San Jose, CA, USA, 2013, pp. 540–547.

[3] V. Mishra and S. S. Sapatnekar, "The impact of electromigration in copper interconnects on power grid integrity," in *Proc. Design Autom. Conf. (DAC)*, Austin, TX, USA, Jun. 2013, pp. 1–6.

[4] I. A. Blech, "Electromigration in thin aluminum films on titanium nitride," *J. Appl. Phys.*, vol. 47, no. 4, pp. 1203–1208, 1976.

[5] J. R. Black, "Electromigration—A brief survey and some recent results," *IEEE Trans. Electron Devices*, vol. 16, no. 4, pp. 338–347, Apr. 1969.

[6] J. R. Lloyd, "New models for interconnect failure in advanced IC technology," in *Proc. Int. Symp. Phys. Failure Anal. Integr. Circuits*, Singapore, 2008, pp. 1–7.

[7] M. Hauschildt *et al.*, "Electromigration early failure void nucleation and growth phenomena in Cu and Cu(Mn) interconnects," in *Proc. IEEE Int. Rel. Phys. Symp. (IRPS)*, Anaheim, CA, USA, 2013, pp. 2C.1.1–2C.1.6.

[8] M. Pathak, J. S. Pak, D. Z. Pan, and S. K. Lim, "Electromigration modeling and full-chip reliability analysis for BEOL interconnect in TSV-based 3D ICs," in *Proc. IEEE/ACM Int. Conf. Comput.-Aided Design (ICCAD)*, San Jose, CA, USA, 2011, pp. 555–562.

[9] X. Huang, T. Yu, V. Sukharev, and S. X.-D. Tan, "Physics-based electromigration assessment for power grid networks," in *Proc. Design Autom. Conf. (DAC)*, San Francisco, CA, USA, Jun. 2014, pp. 1–6.

[10] V. Sukharev, "Beyond Black's equation: Full-chip EM/SM assessment in 3D IC stack," *Microelectron. Eng.*, vol. 120, pp. 99–105, May 2014.

[11] M. A. Korhonen, P. Borgesen, K. N. Tu, and C.-Y. Li, "Stress evolution due to electromigration in confined metal lines," *J. Appl. Phys.*, vol. 73, no. 8, pp. 3790–3799, 1993.

Authorized licensed use limited to: Univ of Calif Riverside. Downloaded on June 24,2026 at 15:12:23 UTC from IEEE Xplore. Restrictions apply.

[12] V. Sukharev, A. Kteyan, E. Zschech, and W. D. Nix, "Microstructure effect on EM-induced degradations in dual inlaid copper interconnects," *IEEE Trans. Device Mater. Rel.*, vol. 9, no. 1, pp. 87–97, Mar. 2009.

[13] (May 20, 2014). *COMSOL Multiphysics*. [Online]. Available: http://www.comsol.com

[14] S. P. Hau-Riege and C. V. Thompson, "Experimental characterization and modeling of the reliability of interconnect trees," *J. Appl. Phys.*, vol. 89, no. 1, pp. 601–609, Jan. 2001.

[15] A. V. Vairagar *et al.*, "Direct evidence of electromigration failure mechanism in dual-damascene Cu interconnect tree structures," *Appl. Phys. Lett.*, vol. 87, no. 8, pp. 081909-1–081909-4, Aug. 2005.

[16] C. V. Thompson, S. P. Hau-Riege, and V. K. Andleigh, "Modeling and experimental characterization of electromigration in interconnect trees," in *AIP Conf. Proc.*, Stuttgart, Germany, 1999, pp. 62–73.

[17] C. L. Gan, C. V. Thompson, K. L. Pey, and W. K. Choi, "Experimental characterization and modeling of the reliability of three-terminal dual-damascene Cu interconnect trees," *J. Appl. Phys.*, vol. 94, no. 2, pp. 1222–1228, Jul. 2003.

[18] S. M. Alam, "Design tool and methodologies for interconnect reliability analysis in integrated circuits," Ph.D. dissertation, Dept. Elect. Eng. Comput. Sci., Massachusetts Inst. Technol., Cambridge, MA, USA, Sep. 2004.

[19] S. P. Hau-Riege and C. V. Thompson, "Electromigration saturation in a simple interconnect tree," *J. Appl. Phys.*, vol. 88, no. 5, pp. 2382–2385, Sep. 2000.

[20] S. P. Hau-Riege, "New methodologies for interconnect reliability assessments of integrated circuits," Ph.D. dissertation, Dept. Mater. Sci. Eng., Massachusetts Inst. Technol., Cambridge, MA, USA, Jun. 2000.

[21] J. J. Clement, S. P. Riege, R. Cvijetic, and C. V. Thompson, "Methodology for electromigration critical threshold design rule evaluation," *IEEE Trans. Comput.-Aided Design Integr. Circuits Syst.*, vol. 18, no. 5, pp. 576–581, May 1999.

[22] A. Abbasinasab and M. Marek-Sadowska, "Blech effect in interconnects: Applications and design guidelines," in *Proc. Int. Symp. Phys. Design (ISPD)*, Monterey, CA, USA, 2015, pp. 111–118.

[23] F. F. Abraham, *Homogeneous Nucleation Theory*. New York, NY, USA: Academic Press, 1974.

[24] Z. Suo, "Reliability of interconnect structures," in *Comprehensive Structural Integrity*, vol. 8. Amsterdam, The Netherlands: Elsevier, 2003.

[25] M. H. Lin and A. S. Oates, "An electromigration failure distribution model for short-length conductors incorporating passive sinks/reservoirs," *IEEE Trans. Device Mater. Rel.*, vol. 13, no. 1, pp. 322–326, Mar. 2013.

[26] V. Sukharev, X. Huang, and S. X.-D. Tan, "Electromigration induced stress evolution under alternate current and pulse current loads," *J. Appl. Phys.*, vol. 118, no. 3, pp. 034504-1–034504-10, 2015.

[27] S. M. Alam, G. C. Lip, C. V. Thompson, and D. Troxel, "Circuit level reliability analysis of Cu interconnects," in *Proc. Int. Symp. Qual. Electron. Design (ISQED)*, San Jose, CA, USA, 2004, pp. 238–243.

[28] C. L. Gan *et al.*, "Experimental characterization of the reliability of multi-terminal dual-damascene copper interconnect trees," in *Mater. Res. Soc. Symp. Proc. (MRSSP)*, 2003, pp. 121–126.

[29] H.-B. Chen, S. X.-D. Tan, V. Sukharev, X. Huang, and T. Kim, "Interconnect reliability modeling and analysis for multi-branch interconnect trees," in *Proc. Design Autom. Conf. (DAC)*, San Francisco, CA, USA, Jun. 2015, pp. 1–6.

Hai-Bao Chen received the B.S. degree in information and computing sciences, and the M.S. and Ph.D. degrees in applied mathematics from Xi'an Jiaotong University, Xi'an, China, in 2006, 2008, and 2012, respectively.

He joined Huawei Technologies, Shenzhen, China, where he focused on cloud computing and big data. He was a Post-Doctoral Research Fellow with the Electrical Engineering Department, University of California, Riverside, CA, USA, from 2013 to 2014. He is currently an Assistant Professor with the Department of Micro/Nano-Electronics, Shanghai Jiao Tong University, Shanghai, China. He has authored or co-authored over 20 papers in scientific journals and conference proceedings. His current research interests include model order reduction, system and control theory, circuit simulation, cloud computing and big data, and electromigration reliability.

Dr. Chen was a recipient of one Best Paper Award Nomination from Asia and South Pacific Design Automation Conference in 2015.

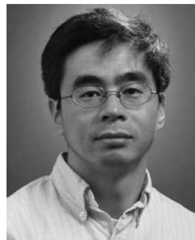

Sheldon X.-D. Tan (S'96–M'99–SM'06) received the B.S. and M.S. degrees in electrical engineering from Fudan University, Shanghai, China, in 1992 and 1995, respectively, and the Ph.D. degree in electrical and computer engineering from the University of Iowa, Iowa City, IA, USA, in 1999.

He is a Professor with the Department of Electrical Engineering, University of California, Riverside, CA, USA, where he is also a Cooperative Faculty Member with the Department of Computer Science and Engineering. He is also a Guest Professor with Shanghai Jiao Tong University, Shanghai, and with the University of Electronic Science and Technology of China, Chengdu China. His current research interests include very large scale integration reliability modeling, optimization and management at circuit and system levels, thermal modeling, optimization and dynamic thermal management for many-core processors, statistical modeling, simulation, and optimization of mixed-signal/RF/analog circuits, parallel circuit simulation techniques based on GPU, and multicore systems.

Prof. Tan was a recipient of the Outstanding Oversea Investigator Award from the National Natural Science Foundation of China in 2008, the NSF CAREER Award in 2004, the Best Paper Award from the 2007 IEEE International Conference on Computer Design, the Best Paper Award from 1999 IEEE/ACM Design Automation Conference, three Best Paper Award Nominations from the IEEE/ACM Design Automation Conferences in 2005, 2009, and 2014, and one Best Paper Award Nomination from ASPDAC in 2015. He is currently serving as the Editor-in-Chief for *Integration, the VLSI Journal*. He is also serving as an Associate Editor for two journals, including the IEEE TRANSACTIONS ON VERY LARGE SCALE INTEGRATION (VLSI) SYSTEMS and *ACM Transaction on Design Automation of Electronic Systems*.

Xin Huang received the B.S. degree from Sichuan University, Chengdu, China, in 2008, and the M.S. degree from Peking University, Beijing, China, in 2011, both in microelectronics. She is currently pursuing the Ph.D. degree in electrical and computer engineering with the University of California, Riverside, CA, USA.

Her current research interests include electromigration modeling and assessment and reliability-aware performance optimization.

Ms. Huang was a recipient of the Best Paper Award from the 2014 IEEE/ACM Design Automation Conference.

Taeyoung Kim received the B.S degree from Konkuk University, Seoul, Korea, in 2005, and the M.S. degree in electrical and computer engineering from the University of Virginia, Charlottesville, VA, USA, in 2012. He is currently pursuing the Ph.D. degree with the Department of Computer Science and Engineering, University of California, Riverside, CA, USA.

His current research interests include embedded system design and reliability-aware system modeling and optimization.

Valeriy Sukharev received the Ph.D. degree in physical chemistry from the Russian Academy of Sciences, Moscow, Russia.

Prior to Mentor Graphics, he was a Chief Scientist with Ponte Solutions, Inc., Mountain View, CA, USA, a Visiting Professor with Brown University, Providence, RI, USA, and a Guest Researcher with the National Institute of Standards and Technology, Gaithersburg, MD, USA. He is the Technical Lead of the Design-to-Silicon Division, Mentor Graphics Corporation, Fremont, CA, USA. He has been with Mentor Graphics Research and Development for seven years. He held senior technical positions with LSI Logic Advanced Development Laboratory, Milpitas, CA, USA. He leads research and development of new full-chip modeling and simulation capabilities for the semiconductor processing and design for manufacturability and reliability applications. He has authored and edited a number of books, published over 100 papers in scientific journals and conference proceedings, and holds more than 20 U.S. patents.

Authorized licensed use limited to: Univ of Calif Riverside. Downloaded on June 24,2026 at 15:12:23 UTC from IEEE Xplore. Restrictions apply.